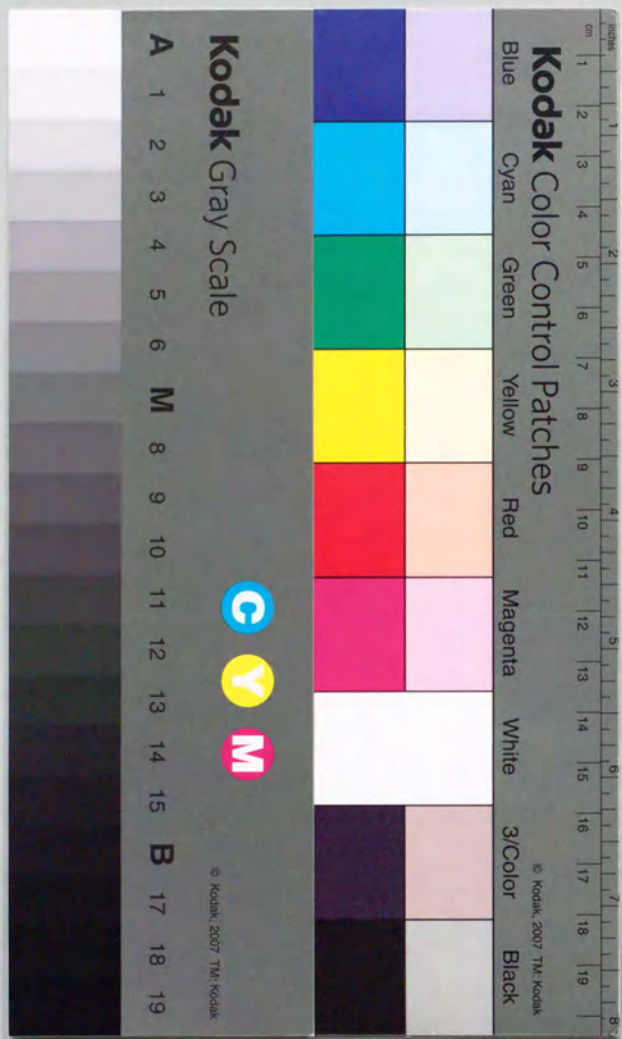


CHARACTERIZATION of MATERIALS
by
X-RAY PHOTOACOUSTIC SPECTROSCOPY
(X線光音響分光法による材料評価の研究)

1991

Kenji KATO



①

Characterization of Materials
by X-ray Photoacoustic Spectroscopy

Kenji KATO
Chemical Analysis and Standard Division,
National Chemical Laboratory for Industry,
Higashi 1-1, Ibaraki, 305 Japan.

A Dissertation
Submitted in Partial Fulfillment of the Requirements
for the Degree of
Doctor of Engineering

at
The University of Tokyo

1991

Preface

The photoacoustic effect was discovered in the latter half of the nineteenth century and was assigned as one of the great scientific achievements of the nineteenth century. Almost 100 years later, the photoacoustic effect was rediscovered and now appears to be well on its way to achieving lasting and significant status. In the 10 years since its "rediscovery" as a new technique for the study of condensed and gaseous matter, photoacoustics already has established itself as an important research and analytical tool in many different fields, including physics, chemistry, biology, and medicine.

This new technique, called photoacoustic spectroscopy (PAS) is based on a heat generation process involving optical absorption in the sample under study, followed by conversion of the absorbed energy into heat. The subsequent heat-induced thermal expansion in the sample and adjacent media produces a photoacoustic signal when the incident beam intensity is modulated at a frequency in the acoustic range.

In photoacoustics, it is the absorption of electromagnetic radiation that gives rise to the acoustic signal. It should be kept in mind that a photoacoustic signal can be generated by absorption of photons in any wavelength region ranging from the high-energy γ -ray region to the low-energy far infrared region. Furthermore, other

energetic beams, such as electrons and ions can generate the photoacoustic effect. However, photoacoustic measurements have been primarily conducted in the UV to IR region.

Recently, photoacoustic measurements in the X-ray region were successfully conducted using a conventional X-ray tube and synchrotron radiation as the excitation source. In the X-ray region, the two most common spectroscopic techniques are X-ray fluorescence spectroscopy and X-ray diffraction. Comparatively, little work has been done on the absorption of X-rays.

It is the purpose of this thesis to describe X-ray photoacoustic spectroscopy for the characterization of materials and to illustrate briefly its basic techniques and wide applicability in the fields of materials science. The first chapter of the thesis covers the photoacoustic theory of condensed materials and an explanation of the interaction between X-rays and matter. In Chapter II, the experimental results of X-ray photoacoustic measurements by excitation with a conventional X-ray tube are presented. In the subsequent chapters, X-ray photoacoustic experiments are applied to the characterization of materials. These include the correlation technique, simultaneous measurements of photoacoustic and fluorescence signals, quantitative analysis, and two-dimensional imaging spectrometry.

Contents

Preface	I
Contents	III
List of Figures	VI
List of Tables	XII
I. Introduction to X-ray Photoacoustic Spectroscopy	1
1-1. Process of Heat Generation Caused by Interaction between the Solid and Photons in the X-ray Region	3
Photoelectric absorption	5
Emission of fluorescent X-rays	6
Compton scattering	8
Rayleigh scattering	11
1-2. Theory of the Photoacoustic Effect in Solids	13
General solution	13
Special cases of photoacoustic signal generation	21
Frequency dependence of photoacoustic signals	25
Depth profiling	25
II. Instrumentation and Detection of X-ray Photoacoustic Signals	27
2-1. Instrumentation for X-ray Photoacoustic Spectroscopy	28
2-1-1. X-ray sources	28
X-ray tube	29
Synchrotron Radiation	30
2-1-2. Photoacoustic Cell	31
2-1-3. Signal Processing System	35
2-2. Photoacoustic Signal Detection under X-ray Tube Excitation	38
Experimental	38
Result and Discussion	40
2-3. Detection of Photothermal Deflection Signals with X-ray Excitation	47
Experimental	48
Results and Discussion	50

III. Correlation Photoacoustics in the X-ray Region	56
3-1. Correlation Photoacoustics	58
Principle of Method	59
Random Chopper	65
Correlation Photoacoustic Spectra of the First Kind	67
Correlation Photoacoustic Spectra of the Second Kind	69
3-2. Correlation Photoacoustic Measurement by Excitation with Synchrotron Radiation (Thermal Properties)	75
Experimental	76
Results and discussion	79
3-3. X-ray Correlation Photoacoustics for Depth Resolved Analysis of Layered Materials	88
Apparatus	89
Sample materials	91
Results and discussion	93
3-4. X-ray Correlation Photoacoustic Spectra near the Absorption Edge	105
Experimental	105
Results and Discussion	106
IV. Simultaneous Measurement of X-ray Photoacoustic and Fluorescence Signals	111
4-1. Simultaneous Detection of X-ray Photoacoustic and Fluorescence Signals as Applied to Characterization of Layered Materials	112
Experimental	112
Results and Discussion	115
4-2. An Approach to the direct Measurement of the Absolute X-ray Fluorescence Quantum Yield	128
Experimental	130
Samples	133
Results and Discussion	133
Procedure for Determining the Fluorescence Quantum Yield	133
Fluorescence Quantum Yield of Uranium-micas	138
Transition Rate Constants for the Radiative and Non-radiative Process	145

4-3. Simultaneous Detection of X-ray Photoacoustic and Fluorescence Signals for Evaluation of Fluorescence Quantum Yield	147
Theoretical	147
Experimental	149
Results and Discussion	149
V. Application to Quantitative Analysis of Powdered Samples	154
5-1. X-ray Photoacoustic Spectrometry Applied to Determination of Iron in Aluminum Hydroxide Gel	156
Experimental	157
Results and Discussion	159
5-2. X-ray Photoacoustic Spectra of Powdered Samples	171
Experimental	171
Results and Discussion	172
VI. X-ray Photoacoustic Imaging of Surface and Subsurface Structure of Layered Materials	178
Experimental	179
Samples	181
Results and Discussion	183
Summary and Future trends	191
References	194
Acknowledgments	200

List of Figures

- Fig. 1. Schematic diagram of photoacoustic signal generation.
- Fig. 1-1-1. Interactions between X-rays and a solid.
- Fig. 1-1-2. Schematic diagram of energy band structure and emission of fluorescent X-rays and Auger electron.
- Fig. 1-2-1. Schematic diagram of a photoacoustic measurement.
- Fig. 1-2-2. Cross-sectional view of a one dimensional simple cylindrical photoacoustic cell.
- Fig. 1-2-3. Six possible cases of photoacoustic signal generation.
- Fig. 2-1-1. Frequency characteristic of a photoacoustic cell.
- Fig. 2-2-1. Photoacoustic cell for X-ray measurement.
- Fig. 2-2-2. Photoacoustic intensities *versus* X-ray tube current.
- Fig. 2-2-3. X-ray spectra of excitation source and transmission spectra of beryllium window.
- Fig. 2-2-4. Photoacoustic intensities *versus* chopping frequency.
- Fig. 2-3-1. Schematic block diagram of photothermal deflection measurement by X-ray excitation.
- Fig. 2-3-2. Photothermal deflection signal intensity recorded on a chart recorder for a copper foil sample.
- Fig. 2-3-3. Photothermal deflection signal intensity *vs.* chopping frequency.
- Fig. 2-3-4. Photothermal deflection signal intensity recorded on a chart recorder for the small angle reflection arrangement and for the parallel arrangement.

Fig. 3-1-1. Block diagram showing the measuring system of correlation photoacoustics.

Fig. 3-1-2. Diagram showing the relation of the input $F(t)$, the output $G(t)$ and the correlation function $C(\tau)$.

Fig. 3-1-3. Silhouette of a random chopper based on an M-series binary sequence ($n=127$).

Fig. 3-1-4. Model samples I and II with a layered structure.

Fig. 3-1-5. The first kind correlation photoacoustic spectra of model sample I.

Fig. 3-1-6. Plots of the delay time τ_0 of model sample I as a function of polyethylene film thickness.

Fig. 3-1-7. Curves of the second kind correlation photoacoustic spectra of model sample II.

Fig. 3-2-1. Schematic diagram of the experimental arrangement.

Fig. 3-2-2. Cross section of the photoacoustic cell designed for measurements in the X-ray region.

Fig. 3-2-3. The first kind correlation spectra of a $10\mu\text{m}$ thick copper foil sample.

Fig. 3-2-4. Dependence of τ_A , τ_0 and τ_f on chopper speed for a $10\mu\text{m}$ thick copper foil sample.

Fig. 3-2-5. Dependence of I_{max} on the correlation spectra of a $10\mu\text{m}$ thick copper foil sample on chopper speed.

Fig. 3-2-6. Changes of τ_0 , τ_A , τ_f and I_{max} of correlation spectra of copper samples *versus* sample thickness.

Fig. 3-2-7. Changes of τ_0 , τ_f and I_{max} for laminated samples versus the number of adhesive films.

Fig. 3-3-1. Schematic diagram of the experimental arrangement.

Fig. 3-3-2. Cross section and top view of the samples of type I, II and III.

Fig. 3-3-3. Correlation photoacoustic spectra (impulse response curves) of type I samples.

Fig. 3-3-4. Dependence of τ_0 of sample type I on the number of the aluminum layers measured at 1.30 and 1.45A.

Fig. 3-3-5. Correlation photoacoustic spectra of type II samples and type III samples measured with white X-ray excitation.

Fig. 3-3-6. Dependence of τ_0 of type II samples and type III samples on the number of polymer layers measured with white X-ray excitation.

Fig. 3-3-7. Correlation photoacoustic spectra of type III samples measured with visible light beam of 2mm and 13mm diameter.

Fig. 3-3-8. Dependence of τ_0 for type III samples on the number of polymer layers measured with a visible light beam of 2mm and 13mm diameter.

Fig. 3-4-1. Dependence of τ_0 on X-ray wavelength for copper foils of 10, 50, 200 and $1000\mu\text{m}$ thickness.

Fig. 3-4-2. Dependence of τ_f on X-ray wavelength for copper foils of 10, 50, 200 and $1000\mu\text{m}$ thickness.

Fig. 3-4-3. Dependence of I_{max} on X-ray wavelength for copper foils of 10, 50, 200 and 1000 μm thickness.

Fig. 4-1-1. A sectional view of the experimental arrangement for a simultaneous X-ray photoacoustic and fluorescence measurements.

Fig. 4-1-2. Photoacoustic and fluorescence signal intensities for different copper foil thicknesses.

Fig. 4-1-3. Log-log plots of photoacoustic signal intensity for different copper foil thicknesses.

Fig. 4-1-4. Phase lag of the photoacoustic signal *versus* the square root of the angular chopping frequency for a laminated specimen of copper and polymer.

Fig. 4-1-5. Phase lag of the photoacoustic signal *versus* the square root of the angular chopping frequency for a laminated specimen of lead and aluminum.

Fig. 4-1-6. Simultaneously measured photoacoustic and fluorescence signals by X-ray excitation for a model specimen.

Fig. 4-1-7. Fluorescence spectra simultaneously measured with the photoacoustic signal at position $X=4, 7$ and 10mm .

Fig. 4-2-1. Block diagram showing the system for simultaneous photoacoustic and fluorescent measurements.

Fig. 4-2-2. Sample cell for simultaneous photoacoustic and fluorescence measurements.

Fig. 4-2-3. An energy diagram tentatively given for deriving the relations in the fluorescence quantum yield calculation.

Fig. 4-2-4. Expected intensities of fluorescent and photoacoustic outputs and their ratio.

Fig. 4-2-5. Energy level diagram showing the excitation and fluorescent transitions for a uranyl(VI) ion.

Fig. 4-2-6. Fluorescent emission spectra, fluorescent excitation spectra and photoacoustic spectra of $\text{Ba}(\text{UO}_2)_2(\text{PO}_4)_2 \cdot n\text{H}_2\text{O}$.

Fig. 4-2-7. Plots of the intensity ratios of photoacoustic and fluorescent excitation signal intensities.

Fig. 4-3-1. A schematic diagram of the experimental setup and the photoacoustic cell for simultaneous measurements.

Fig. 4-3-2, A. Simultaneously measured photoacoustic and fluorescence excitation spectra for a $10\mu\text{m}$ thick copper sample.

Fig. 4-3-2, B. Plots of the ratio of photoacoustic and fluorescent signal intensities.

Fig. 5-1-1. Side view of the photoacoustic cell for measurement of the powder samples.

Fig. 5-1-2A. Results of thermogravimetric and differential thermal analysis for sample No-1.

Fig. 5-1-2B. Results of thermogravimetric and differential thermal analysis for sample No-4.

- Fig. 5-1-3. Photoacoustic intensities *versus* iron content for various chopping frequencies.
- Fig. 5-1-4. Corrected photoacoustic intensities *versus* iron content for various chopping frequencies.
- Fig. 5-1-5. Photoacoustic intensities *versus* chopping frequency.
- Fig. 5-1-6A, B. Microphotographs of powdered samples No-1 and 2.
- Fig. 5-1-6C, D. Microphotographs of powdered samples No-3 and 4.
- Fig. 5-2-1. X-ray photoacoustic spectra near the Fe-K absorption edge.
- Fig. 5-2-2. Estimated X-ray photoacoustic spectra of iron sponge powder.
- Fig. 5-2-3. Estimated X-ray photoacoustic spectra of active alumina powder with 1.72% iron.
- Fig. 6-1. Schematic diagram of the experimental set up for X-ray photoacoustic imaging.
- Fig. 6-2. Photographs of a flexible printed circuit board.
- Fig. 6-3. X-ray photoacoustic images of the lead / aluminum laminated sample.
- Fig. 6-4. Visible light photoacoustic images of the lead / aluminum laminated sample.
- Fig. 6-5. X-ray photoacoustic images of the flexible printed circuit board.
- Fig. 6-6. Photoacoustic images of the flexible printed circuit board with UV light excitation.

List of Tables

- Table 2-1-1. Synchrotron radiation beam at Photon Factory (KEK) and their performance.
- Table 4-2-1. Data of Quantum Yield Q_F , Fluorescence life time τ , and transition rate constants k_r and k_n of the respective radiative and non-radiative processes for a series of uranium mica compounds $M(UO_2)_2(XO_4)_2 \cdot H_2O$.
- Table 5-1-1. Iron and water contents in samples.

CHAPTER I

Introduction to X-ray Photoacoustic Spectroscopy

The photoacoustic method is based on the measurement of the acoustic wave caused by the absorption of modulated optical radiation. It can be conducted using any type of energetic radiation, including electromagnetic radiation ranging from radio waves to X-rays, as well as electrons, protons, ions and other particles. The radiation energy absorbed by a solid is converted, in part or in whole, into heat through nonradiative decay processes within the solid. Figure 1 is a schematic diagram of generation of photoacoustic signal caused by X-ray excitation. When the incident X-ray beam is periodically modulated, periodic heat is generated in the sample. This modulated heat causes a pressure fluctuation in the surroundings, which is detected by a microphone as an acoustic wave. The heat generation followed by absorption of photons is a matter of primary concern in the photoacoustic method. So far, in the field of X-ray spectroscopy, little attention has been paid to the heat generation by X-ray absorption. Therefore, the process of heat generation in X-ray absorption will be discussed in section 1-1 followed by a general theoretical presentation of photoacoustic signal generation in section 1-2.

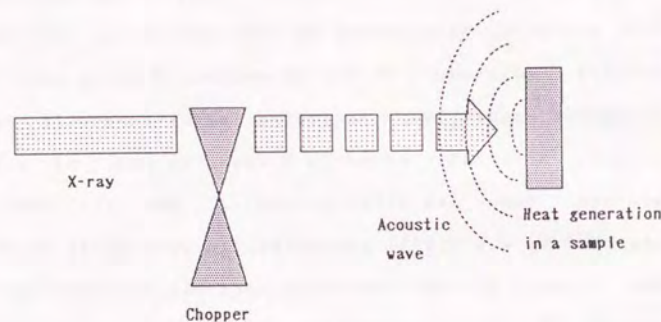


Fig. 1. Schematic diagram of photoacoustic signal generation caused by irradiation of chopped X-ray beam.

1-1 Process of Heat Generation Caused by Interaction between the Solid and Photons in the X-ray Region.

Irradiation of X-rays causes a variety of phenomena in solids as shown in Fig. 1-1-1. Emission of electrons (Auger electrons and photoelectrons) is a result of X-ray absorption or the result of non-elastic X-ray scattering. The kinetic energy of the emitted electron is then converted to heat in the course of collisions in the solid or in the surrounding atmosphere. In the process of electron emission a polarized state such as an electron-hole pair is formed in the solid. Polarized state disappears by electron-hole recombination with heat being released. The rate of this recombination depends on the mobility of both the electron and the hole in the solid. If the mobility is low, heat released in this process will have a long life time. And, if the electrons is transmitted out of the solid as photocurrent, the heat release will diminish. The emission of fluorescence X-rays takes out part of the absorbed energy. The fluorescent X-rays are, in part, absorbed in the solid and also generates heat. Thus, heat generation caused by interaction between the solid and photon in the X-ray region is related to several effects and the total amount of heat generation excited by monochromated X-rays, $H(E)$ can be expressed as follows;

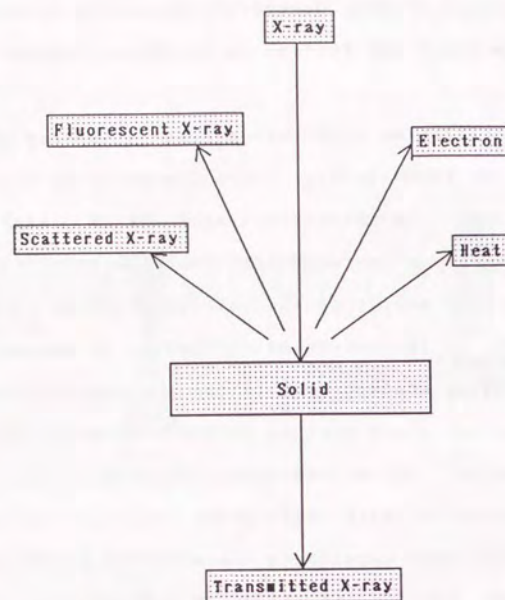


Fig. 1-1-1. Interactions between X-rays and a solid.

$$H(E) = I_0(E) \{ P(E) + F(E) + N(E) \}, \quad (1.1.1)$$

where I_0 , P , F , N and E are the intensity of the incident X-ray beam, efficiency of X-ray photoelectric absorption, efficiency of heat loss by emission of fluorescent X-rays, heat emission by non-elastic scattering and photon energy of the incident X-rays. Contribution of each process in the range of about 1 to 100 KeV is discussed in the following paragraphs.

Photoelectric absorption

Lambert-Beer's law applies in the X-ray region. The ratio between the incident and transmitted X-ray intensity can be calculated using of X-ray extinction coefficients. Therefore, contribution of the photoelectric absorption to the heat release is given by the following equation;

$$P(E) = \{ 1 - \exp(-t \mu(E) \rho) \} E, \quad (1.1.2)$$

where t , $\mu(E)$ and ρ are the thickness of the solid, mass absorption coefficient of the solid and density of the solid, respectively. The mass absorption coefficient, μ , is generally given by¹⁾

$$\mu(E) = \tau(E) + \sigma / \rho \quad (1.1.3)$$

and

$$\tau(E) = C E^{-3} - D E^{-4}, \quad (1.1.4)$$

where $\tau(E)$ and σ are the photoelectric absorption and the scattering loss of the X-ray beam respectively. Discussion

about scattering will be given in the following section. Parameters C and D are functions of atomic number. It is clear from Eqn. 1.1.4 that photoelectric absorption is negligible for light atoms and for high energy X-rays. Usually the interaction dominates for X-rays and matter in the range below 100KeV and is negligible above 1MeV.

Emission of fluorescent X-rays

Excitation of the solid is achieved by irradiation of photons with energy greater than the absorption edge of a particular characteristic fluorescent X-rays. A schematic diagram of the fluorescent X-ray process is shown in Fig. 1-1-2. For example, when the energy of the primary X-rays exceeds the K-absorption edge energy, a vacancy is created in the K-electron band and an electron in the L-electron band fills the vacancy. In this process, two kinds of phenomena will occur: electron emission from the L-band (KLL Auger process) and X-ray (K_{α} fluorescent X-rays) emission. The fluorescent X-rays carry away some energies from the solid. The heat loss by emission of fluorescent X-rays is complicated, because the solid may radiate various fluorescent X-rays and the fluorescent X-rays may be absorbed in the solid itself. The heat release by fluorescence is given by

$$F(E) = \{1 - \exp(-t \mu(E) \rho)\} \sum (\Delta E_n Q_{fn} K_n(E)) \quad (1.1.5)$$

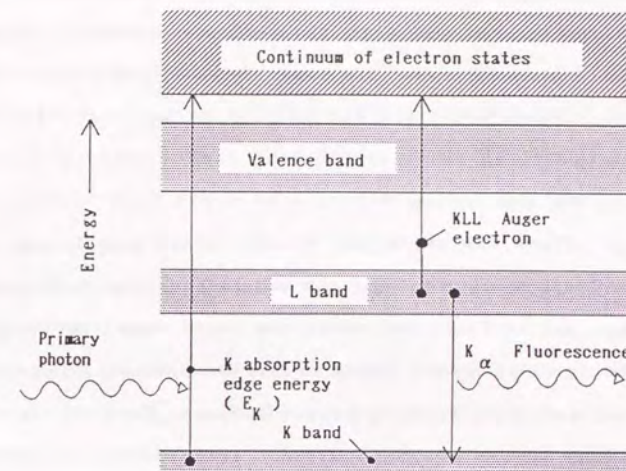


Fig.1-1-2. Schematic diagram of energy band structure and emission of fluorescent X-rays and Auger electron.

where t , $\mu(E)$ and ρ are the thickness, mass absorption coefficient, density of the solid, and ΔE_n , Q_{rn} and $K_n(E)$ are energy, quantum yield and correction factor for self absorption of the n -th fluorescence X-rays, respectively. The fluorescence quantum yield are given in the literatures^{2, 3}.

Compton scattering

There are two kinds of scattering processes, incoherent or Compton scattering, and coherent or Rayleigh scattering. The latter is described in the next section. Compton scattering arises from collision between a photon and a comparatively loosely bound electron. Part of the collision energy is transferred to the electron, and the energy of the scattered photon is accordingly modified. In the high energy region non-elastic scattering often dominates the interaction between X-rays and matters, particularly for light elements⁴. In this case, the energy transferred, ΔE to the electron must be calculated relativistically and is given by

$$\Delta E = 2E^2 (1 - \cos\phi) / (2E + m_e c^2), \quad (1.1.6)$$

where E , ϕ , m_e and c are the energy of the photon, the scattering angle, the electron rest mass and the velocity of light, respectively. The maximum energy ($\phi=180^\circ$) transferred to an electron by a 10KeV photon (wavelength of

1.24Å) is about 400eV, in which case the photon wavelength would shift to a longer wavelength by 0.05Å after scattering. No interference takes place between radiation scattered by different electrons of the materials. Compton scattering, however, depends on the wave-function of individual electrons which for valence electrons depend on the chemical binding. The probability that a Compton scattering event will occur is expressed in terms of an extinction coefficient σ for the solid, which was shown in the previous Eqn. 1.1.3. Compton scattering depends on the wave-function of individual electrons which for valence electrons depend on the chemical binding. Nevertheless, it may be seen that for not too long wavelengths, the additivity relations for Compton scattering holds to a very good approximation. If the number of electrons per unit volume in the solid and the cross-section per electron are denoted as N_e and σ_e respectively, σ is expressed as

$$\sigma = N_e \sigma_e. \quad (1.1.7)$$

The intensity of unscattered photons after passage through a thickness t of the solid is then given by

$$I(t) = I_0 \exp(-\sigma t). \quad (1.1.8)$$

The number of electrons per unit volume is given by

$$N_e = N_A \rho (Z/M), \quad (1.1.9)$$

where N_A , ρ , Z and M are Avogadro's number, density, atomic number and atomic weight of the scatterer, respectively.

(Z/M) is 1 for Hydrogen and about 0.4 for Uranium. While the photoelectric absorption coefficient varies as a function of Z^4 and E^{-3} , Compton scattering is important for light atoms and for high energy photons. For Compton scattering of low energy, the cross-section per electron is given by

$$\sigma_e = \sigma_{e0} = \frac{e^4}{6 \pi \epsilon_0^2 m_e^2 c^4}, \quad (1.1.10)$$

where ϵ_0 is the permittivity of free space, and is estimated to be $6.7 \times 10^{-29} \text{ m}^2$. At high photon energies, the cross-section per electron is given by

$$\sigma_e = \sigma_{e0} \frac{3}{8 E'} \left\{ \frac{1}{2} + 2 \ln(2 E') \right\}, \quad (1.1.11)$$

where $E' = E/m_e c^2$. This changes much more slowly as a function of wavelength than either the photoelectric or the elastic scattering cross-section and for that reason it often dominates photon-atom interactions in the 100KeV to 1MeV range. But, for X-rays in the 0.5-40KeV region, σ is small as compared to the photoelectric absorption coefficient. Furthermore, ΔE is also small. For example, σ for copper metal for a 40KeV X-ray is about 140 m^{-1} and is small compared to the photoelectric absorption coefficient ($3.9 \times 10^9 \text{ m}^{-1}$). The energy loss ΔE is also about 5KeV. Therefore, the heat emission by Compton scattering is negligible in this study. However, the process is important for light metals used for a window materials such as Be. In

this case, the heat generated by Compton scattering is larger than that for photoelectric absorption.

Rayleigh scattering

Photons can also scatter from atoms within the sample. If the energy of the photon is small enough, it can interact with the atom as a whole, and is then scattered with very little loss of energy, which is also called Thomson scattering⁴³. The maximum energy which can be lost to an atom in this way can be calculated very easily, provided we remember that the momentum of a photon of energy E is E/c , where c is the velocity of light. The maximum energy transfer occurs when the photon scattered backwards. From the momentum conservation law and the energy conservation law the energy loss, ΔE , is approximately given by

$$\Delta E = 2E^2 / (m c^2), \quad (1.1.12)$$

where m is the mass of the particle. Since the term mc^2 is about 900MeV even for a hydrogen atom, it is clear that the assumption of small energy transfer is reasonable for all photon energies. This scattering is often also called coherent or elastic scattering because ΔE is very small. It is very unlikely that E is large because it requires that the photon first interacts with the electrons in the atom and that these in turn interact with the nucleus. For high

photon energies it becomes more probable that the photon will tear one of the electrons off the atom as the interaction occurs. For example, the probability of elastic scattering of KeV photons by carbon atoms is negligible, yet even under these conditions the maximum energy transfer is very small as estimated from Eqn. 1.1.12. For this reason Rayleigh scattering is not important as a heat generating process and is negligible in the X-ray region below 100KeV.

1-2 Theory of the Photoacoustic Effect in Solids.

Figure 1-2-1 is a schematic diagram of the photoacoustic measurement system. The acoustic wave that arises from the periodic heating of the gas is detected by a microphone. The gas in contact with the sample irradiated with a chopped exciting beam. Various types of signal detection techniques use in photoacoustic measurements have been reviewed by Tam⁶⁾. Rosencwaig and Gersho presented a general theory (RG theory) for photoacoustic signal generation in solids^{6, 7)}.

General solution

It is assumed in RG theory that the acoustic signal results from a periodic heat flow from the solid to the surrounding gas. The solid is cyclically heated by absorption of the chopped light in the one dimensional simple cylindrical cell like the one shown in Fig. 1-2-2. The photoacoustic cell has a diameter r and length L . L is assumed to be smaller than the wavelength of the acoustic wave. The microphone detects the average pressure produced in the cell. Assuming that the incident beam of radius r is modulated at angular frequency ω , the intensity will be given by

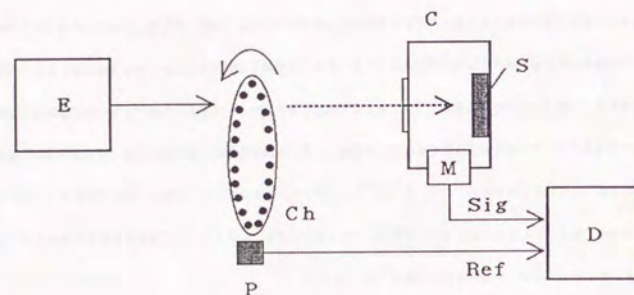


Fig.1-2-1. A schematic diagram of a photoacoustic measurement.

E, excitation beam; Ch, rotating chopper;
P, photocoupler used for generating a reference
signal; C, photoacoustic cell; S, sample;
M, microphone; D, signal detecting system.

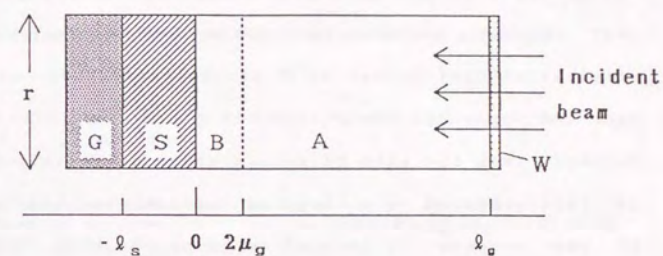


Fig.1-2-2. Cross-sectional view of a one dimensional simple cylindrical photoacoustic cell.

A, gas (air); B, boundary layer of gas; S, sample;
G, semi-infinite substrate; W, cell window.

$$I = \frac{1}{2} I_0 \{1 + \cos(\omega t)\}, \quad (1.2.1)$$

where I_0 is the incident light flux. The sample is assumed to have a disc shape with diameter r and thickness l_s , and is mounted so that the back surface is in contact with a poor thermal conductor substrate. Let the sample optical attenuation coefficient be β at the excitation wavelength, and the optical absorption length be $\mu \beta = 1/\beta$. It is assumed that the rate of nonradiative deexcitation process is fast compared to a chopping period, and the efficiency of the process is assumed to be unity. The heat $H(x, t)$ produced at depth x ($-l_s < x < 0$) within the sample is given by

$$H(x, t) = \frac{1}{2} \beta I_0 \{1 + \cos(\omega t)\} \exp(\beta x). \quad (1.2.3)$$

Parameters concerning the heat diffusion are defined as follows:

k : the thermal conductivity,

ρ : the density,

C : the specific heat,

$\alpha = k/\rho C$: the thermal diffusivity,

$a = (\omega/2\alpha)^{1/2}$: the thermal diffusion coefficient,

$\mu = 1/a$: the thermal diffusion length.

The subscripts s, g and b represent parameters for the sample, the gas and the substrate, respectively. Taking into account the distributed heat source, the thermal diffusion

equation in the solid can be written as

$$\frac{\partial^2 \phi}{\partial x^2} = \frac{1}{\alpha_s} \frac{\partial \phi}{\partial t} - \frac{\beta I_0}{2k} \{1 + \exp(i\omega t)\} \exp(\beta x) \quad \text{for } -l_s \leq x \leq 0, \quad (1.2.4)$$

where ϕ is the temperature. For the substrate and the gas, the heat diffusion equations are respectively given by

$$\frac{\partial^2 \phi}{\partial x^2} = \frac{1}{\alpha_b} \frac{\partial \phi}{\partial t} \quad \text{for } -(l_s + l_b) \leq x \leq -l_s, \quad (1.2.5)$$

$$\frac{\partial^2 \phi}{\partial x^2} = \frac{1}{\alpha_g} \frac{\partial \phi}{\partial t} \quad \text{for } 0 \leq x \leq -l_s. \quad (1.2.6)$$

The temperature $T(x, t)$ at position x and time t is given by

$$T(x, t) = \text{Re}\{\phi(x, t)\} + \Phi, \quad (1.2.7)$$

where Φ is the ambient temperature and Re is the real part of the $\phi(x, t)$. The general solution for Eqns. 1.2.4, 1.2.5 and 1.2.6 can be written as

$$\phi(x, t) = (1 - x/l_s) \theta_0 + \theta \exp(-\sigma_g x + i\omega t) \quad \text{for } 0 \leq x \leq -l_s, \quad (1.2.8)$$

where θ_0 and θ are real and imaginary valued constants and $\sigma_g = (1+i)a_g$. Taking into account the continuity of temperature and heat flux at the interfaces and additional boundary conditions, θ is obtained which is a time-dependent component of temperature and contributes to the photoacoustic signal. θ can be expressed as

$$= \frac{\beta I_0 \theta}{2k(\beta^2 - \sigma_{\text{m}}^2)} \times \frac{(r-1)(b+1)\exp(\sigma_{\text{m}} l) - (r+1)(b-1)\exp(-\sigma_{\text{m}} l) + 2(b-r)\exp(-\beta l)}{(g+1)(b+1)\exp(\sigma_{\text{m}} l) - (g-1)(b-1)\exp(\sigma_{\text{m}} l)} \quad (1.2.9)$$

where

$$b = \frac{k_{\text{b}} a_{\text{b}}}{k_{\text{m}} a_{\text{m}}}, \quad g = \frac{k_{\text{g}} a_{\text{g}}}{k_{\text{m}} a_{\text{m}}}, \quad r = (1-i) \frac{\beta}{2a_{\text{m}}},$$

and $\sigma_{\text{m}} = (1-i)a_{\text{m}}$. Thus θ can be evaluated for specific parameter values. The temperature distribution in the gas phase $\phi_{\text{m}}(x, t)$ is given by

$$\phi_{\text{m}}(x, t) = \theta \exp(-\sigma_{\text{m}} x + i\omega t). \quad (1.2.10)$$

If the real and imaginary part of the complex number θ is given by θ_1 and θ_2 , respectively, the actual temperature variation $T_{\text{m}}(x, t)$ in the gas phase is given by

$$T_{\text{m}}(x, t) = \exp(-a_{\text{m}} x) \{ \theta_1 \cos(\omega t - a_{\text{m}} x) - \theta_2 \sin(\omega t - a_{\text{m}} x) \}. \quad (1.2.11)$$

Since the time-dependent component of the temperature in the gas attenuates rapidly to zero with increasing distance from the surface of the solid, at a distance of $2\pi\mu_{\text{m}}$, the periodic temperature variation in the gas is effectively fully damped out. Thus the boundary layer can be defined as shown in Fig. 1-2-2, whose thickness is $2\pi\mu_{\text{m}}$ so that we

can, to a good approximation, assume that only the gas is capable of responding thermally to periodic temperature variations at the sample surface. The spatially averaged temperature $\phi_{\text{mve}}(t)$ of the gas within this boundary layer is obtained as a function of time by integrating Eqn. 1.2.11 from $x=0$ to $2\pi\mu_{\text{m}}$ as

$$\phi_{\text{mve}}(t) = \frac{1}{2\pi\mu_{\text{m}}} \int_0^{2\pi\mu_{\text{m}}} \phi_{\text{m}}(x, t) dx. \quad (1.2.12)$$

From Eqn. 1.2.10 we have

$$\phi_{\text{mve}}(t) \sim \frac{1}{2^{3/2}\pi^{1/2}} \theta \exp\{i(\omega t - \pi/4)\}, \quad (1.2.13)$$

using the approximation $\exp(-2\pi) \ll 1$. Because the boundary layer is periodically heated, this layer of gas expands and contracts periodically and thus can be considered as acting as an acoustic piston on the rest of the gas column, producing an acoustic pressure signal that travels through the entire gas column. The displacement $\delta x(t)$ of this piston due to the periodic heating can be simply estimated by using the ideal gas law as

$$\delta x(t) = 2\pi\mu_{\text{m}} \phi_{\text{mve}}(t) / T_0 = (\theta \mu_{\text{m}} / 2^{1/2} T_0) \exp\{i(\omega t - \pi/4)\}, \quad (1.2.14)$$

where $T_0 = \Phi + \theta$. The pressure variation $\delta P(t)$ in the cell is

derived as $\delta P(t) = \gamma P_0 \delta V / V_0 = \gamma P_0 \delta x(t) / l_{\Sigma}$ from the adiabatic gas law, where γ , P_0 , V_0 and δV are the ratio of the specific heats, the ambient pressure, the cell volume and the variation of cell volume due to the displacement of the piston. From Eqns. 1.2.13 and 1.2.14 we obtain

$$\delta P(t) = Q \exp\{i(\omega t - \pi/4)\}, \quad (1.2.15)$$

where

$$Q = \gamma P \theta_0 / (2^{1/2} l_{\Sigma} a_{\Sigma} T_0). \quad (1.2.16)$$

Thus the actual physical pressure variation, $\Delta p(t)$, is given by the real part of $\delta P(t)$ as

$$\Delta p(t) = Q_1 \cos(\omega t - \pi/4) - Q_2 \sin(\omega t - \pi/4) \quad (1.2.17)$$

or

$$\Delta p(t) = q \cos(\omega t - \phi - \pi/4) \quad (1.2.18)$$

where Q_1 and Q_2 are the real and imaginary parts of Q , and q and $-\phi$ are the magnitude and phase of Q . On finally combining Eqns. 1.2.9 and 1.2.16, the sinusoidal pressure variation Q in the cell is given as

$$\theta = \frac{\beta I_0 \gamma P_0}{2^{3/2} T_0 k_{\Sigma} l_{\Sigma} a_{\Sigma} (\beta^2 - \sigma_{\Sigma}^2)} \times \frac{(r-1)(b+1) \exp(\sigma_{\Sigma} l) - (r+1)(b-1) \exp(-\sigma_{\Sigma} l) + 2(b-r) \exp(-\beta l)}{(g+1)(b+1) \exp(\sigma_{\Sigma} l) - (g-1)(b-1) \exp(\sigma_{\Sigma} l)} \quad (1.2.19)$$

Special cases of photoacoustic signal generation.

The full expression for $\Delta p(t)$ is somewhat difficult to interpret. By examining special cases, the expression for Q becomes relatively simple. Rosencwaig and Gersho classified these cases according to the optical absorption length and the thermal diffusion length^{6, 8}. Six cases are shown in Fig. 1.2.3. In the case where the sample thickness, l_{Σ} is smaller than the optical absorption length, $1/\beta$, the sample is optically transparent and the incident light is absorbed throughout the length of the sample. In the case where l_{Σ} is larger than $1/\beta$, the sample is optically opaque and the incident light is absorbed completely in the sample. In the case where the thermal diffusion length μ_{Σ} is larger than l_{Σ} , the sample is thermally transparent and the heat generated at any position in the sample contributes to photoacoustic signal generation. In the case where the thermal μ_{Σ} is smaller than the l_{Σ} , the sample is thermally opaque and the heat generated only within depth μ_{Σ} contributes to the photoacoustic signal. For all cases it is assumed that $G < b$ and $b \sim 1$, which are rewritten as $k_{\Sigma} a_{\Sigma} < k_b a_b$ and $k_{\Sigma} a_{\Sigma} \sim k_b a_b$.

It is convenient to define $Y = \gamma P_0 I_0 / (2^{3/2} T_0 l_{\Sigma})$.

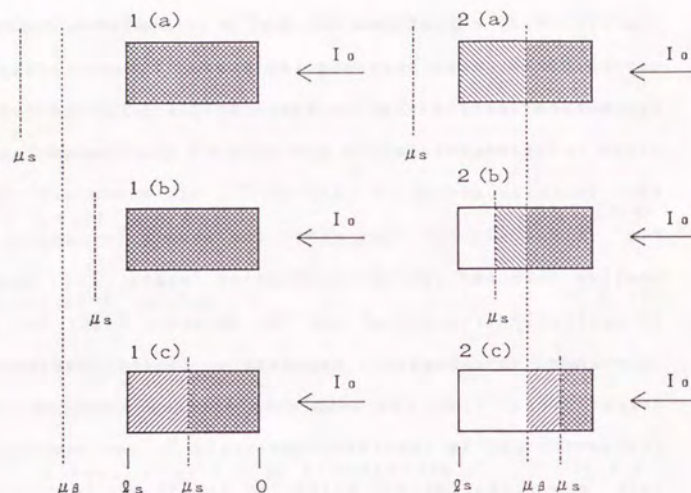


Fig. 1-2-3. Six possible cases of photoacoustic signal generation depending on the relative magnitude of the sample thermal diffusion length μ_s , sample optical absorption length μ_β and sample thickness l_s . The incident beam of intensity I_0 irradiates the sample from the right.

Case 1(a) and 1(b)

These are the cases where the sample is optically or thermally transparent and

$$Q \sim \frac{(1-i) \beta l_s}{2 a_s} (\mu_\beta / k_\beta) Y. \quad (1.2.20)$$

The acoustic signal is proportional to βl_s , and since μ_β / a_s is proportional to ω^{-1} , the acoustic signal has an ω^{-1} dependence. The thermal properties of the substrate come into play in Q .

Case 1(c)

This is the case where the sample is optically transparent but thermally opaque. Q is given as

$$Q \sim \frac{-i \beta \mu_s}{2 a_s} (\mu_s / k_s) Y. \quad (1.2.21)$$

The acoustic signal is proportional to $\beta \mu_s$ rather than βl_s . Since μ_s / a_s is proportional to $1/\omega$ and μ_s is proportional to $\omega^{-1/2}$, the acoustic signal has an $\omega^{-3/2}$ dependence. The thermal properties of the sample come into play in Q .

Case 2(a)

In this case, the sample is optically opaque but thermally transparent and

$$Q \sim \frac{(1-i)}{2a_s} (\mu_b/k_b) Y. \quad (1.2.22)$$

The acoustic signal is independent of βl_s , and since μ_b/a_s is proportional to $1/\omega$, the acoustic signal has an ω^{-1} dependence. The thermal properties of the substrate come into play in Q .

Case 2(b)

In this case, the sample is optically and thermally opaque ($\mu_s > 1/\beta$) and

$$Q \sim \frac{(1-i)}{2a_s} (\mu_s/k_s) Y. \quad (1.2.23)$$

The acoustic signal is independent of βl_s , and since μ_s/a_s is proportional to $1/\omega$, the acoustic signal has an ω^{-1} dependence. The thermal properties of the sample come into play in Q .

Case 2(c)

In this case, the sample is optically and thermally opaque ($\mu_s < 1/\beta$) and

$$Q \sim \frac{-i \beta \mu_s}{2a_s} (\mu_s/k_s) Y. \quad (1.2.24)$$

The acoustic signal is proportional to $\beta \mu_s$ rather than

βl_s , and since μ_s/a_s is proportional to $1/\omega$ and μ_s is proportional to $\omega^{-1/2}$, the acoustic signal has an $\omega^{-3/2}$ dependence. The thermal properties of the sample come into play in Q . In this case we can obtain the optical properties for the optically opaque sample.

Frequency dependence of photoacoustic signals

Intensity of the photoacoustic signal, as mentioned in the previous section, is dependent on the chopping frequency ω . In the case where $\mu_s < l_s$ and $\mu_s < 1/\beta$ (cases 1(c) and 2(c) in the previous section) the acoustic signal has an $\omega^{-3/2}$ dependence. In the other cases, the acoustic signal has an ω^{-1} dependence. This is because $\mu_s = (\omega/2\alpha)^{1/2} = \{2k_s/(\rho C\omega)\}^{1/2}$, so μ_s varies with ω . Thus considering the change in ω dependence of the photoacoustic signal intensity on the chopping frequency, we can obtain information about the thermal properties of a sample.

Depth profiling

In photoacoustic measurements, the phase delay of the signal with respect to the exciting signal offers various information about the sample. Attempts to obtain information about the thermal conductivity or about the layered structure of a material has been of considerable

interest. Adams and Kirkbright⁸⁾ discussed the relation between the phase and the modulation frequency ω for a sample with a simple double-layered structure. Assuming that the upper layer is optically and thermally thin, the signal Q is given by

$$Q = \frac{\beta_1 I_0}{\rho_2 C_2 \omega \mu_2} \exp(-x/\mu_2) \cos(\omega t - \frac{x}{\mu_2} - \frac{\pi}{4}) \quad (1.2.25)$$

where subscript 1 and 2 denotes the parameter of the bottom and upper layers, respectively. The additional phase delay due to the upper layer $\Delta\theta$ is expressed as

$$\Delta\theta = -\frac{x}{\mu_2} = -x (1/2\alpha_2)^{1/2} \omega^{1/2}, \quad (1.2.26)$$

where x and α_2 are the thickness and the thermal diffusivity of the upper layer. By the relation between the relative phase angle and the square root of the modulation frequency, information concerning the thermal diffusivity α or the thickness x of the upper layer can be obtained.

CHAPTER II

Instrumentation and Detection of X-ray Photoacoustic Signals

In the measurement of X-ray photoacoustic signals, it is very important to detect the signals with high signal to noise ratio. Particularly, in the X-ray region, the flux intensity of excitation is weak as compared to that of conventional visible light source. In section 2-1, design of a photoacoustic cell for achieving high sensitivity and low noise measurement will be presented. Section 2-2 is based on a previously published report,⁹⁾ where the first demonstration of photoacoustic measurement in the X-ray region using an X-ray tube is presented. Section 2-3 is based on a previously published report,¹⁰⁾ which reports on the first successful results of photothermal deflection measurements by X-ray excitation.

2-1 Instrumentation for X-ray Photoacoustic Spectroscopy.

The photoacoustic measurement system consists of 3 parts, excitation source, photoacoustic cell, and signal processing system, as shown in the previous chapter. The photoacoustic signal from the microphone is preamplified and a particular signal component having a frequency equal to the chopping frequency is detected by the use of a lock-in amplifier. This section presents a procedure for achieving high sensitivity and low noise photoacoustic measurements. The photoacoustic measurements described in the following chapters were conducted using this procedure.

2-1-1 X-ray sources

The amount of the heat produced in the photoacoustic cell is proportional to the amount of photons falling on the sample. Sensitivity of the photoacoustic cell as a transducer is relatively low compared to that of photomultiplier or semiconductor detector for photons, although the microphone used is very sensitive. Therefore, in the photoacoustic measurements, intensity of the excitation source is very important factor. As mentioned in the next section, X-ray flux of about 0.1 to 1 mW is necessary for the photoacoustic measurements. At present, X-

ray tubes, synchrotron radiation can be used as X-ray sources for photoacoustic measurements. In the near future, X-ray laser and laser plasma X-ray (LAPLAX) which are now developing will be available¹⁰⁻¹⁴.

X-ray tube

X-ray tube is widely available as X-ray source in laboratory. X-ray beam from X-ray tube is divergent and not monochromatic. X-ray tube, however, is useful for particular purposes such as measurements of thermal properties or observation of layered structure (Section 3-2). In particular, X-ray photoacoustic measurements using a conventional X-ray tube as an excitation source can be easily conducted, and is very convenient when combined with other techniques such as X-ray fluorescence (Section 4-1).

X-ray beam from X-ray tube is divergent, therefore, X-ray power at the sample position is inversely proportional to square of distance between the target of the X-ray tube and the sample, and is proportional to the cross section of the sample. The efficiency of the X-ray production, η is estimated by simple formula²⁾.

$$\eta = \frac{\text{X-ray energy}}{\text{cathode ray energy}} = k Z V \quad (2-1-1)$$

where k , Z and V are experimental constant, atomic weight of

the target material and the voltage applied to the X-ray tube. k value is reported to be 20×10^{-10} , 5.6×10^{-10} , 7.2×10^{-10} or 15.0×10^{-10} . For example, available X-ray power at sample position is estimated to be 2.4mW under the conditions: copper target ($Z=29$), electric power of 40KV and 40mA, the distance $l=70\text{mm}$ between the target and the sample, the radius $r=5\text{mm}$ of the photoacoustic cell window, and the efficiency of X-ray generation η (10×10^{-10}).

Available wavelength region of X-rays depends on target material of the X-ray tube, and the wavelength distribution can be modified by voltage applied to the X-ray tube or by the use of filters. But, use of a monochromator is difficult, because of low intensity of the X-ray and low efficiency of the monochromator.

Synchrotron Radiation

In the photoacoustic study in X-ray region, elemental analysis would be possible using the characteristic X-ray absorption. For this purpose, synchrotron radiation is a suitable X-ray source in terms of its wide wavelength selectivity. As described in section 3-4, 4-3 and chapter 5, wavelength selectivity is important in the photoacoustic spectroscopy. The synchrotron radiation is moreover excellent because of its high brightness and directional

nature. At present synchrotron radiation is most useful and powerful soft X-ray source.

X-ray power at the sample position is estimated from the photon flux of the source, the photon energy and the cross section of the beam. Performance of the synchrotron radiation at the Photon Factory (National Laboratory for High energy Physics (KEK), Tsukuba) is listed in Table 2-1-1. For example, the available X-ray power at the sample position is about 0.13mW under the conditions that: beam line BL-15A, photon energy of 8 KeV, synchrotron ring current of 300mA.

The main drawback of synchrotron radiation lies in the fact that these storage ring facilities are not easily accessible. This difficulty will not be solved in the near future. On the contrary, importance of synchrotron radiation is increasing, because new types of insertion devices such as undulator and wiggler are developing and will soon be available. Brilliance of synchrotron radiation using the undulator or the wiggler becomes 10 to 10^3 times that for the conventional synchrotron radiation with bend magnets¹⁶⁾.

2-1-2 Photoacoustic Cell

Since samples used in this study are solid or powder form, the most common and most versatile photoacoustic cell

Table 2-1-1. Synchrotron radiation beam lines and their performance at the Photon Factory (KEK)¹⁶⁾.

Beam line	Beam size	Photon flux	Energy	
			Range (KeV)	Resolution ($\Delta E/E \times 10^4$)
BL-4A	50mmx4mm	—	4-20	2
BL-10C	6mmx1.5mm	10^{10} - 10^{11} photons (8KeV, 100mA)	4-10	2
BL-15A	2.6mmx1.3mm	5×10^{10} photons (8KeV, 150mA)	5.6-12.4	10

will be a gas-microphone cell. The gas-microphone cell generally incorporate a suitable microphone with its preamplifier. Some criteria governing the actual design of the photoacoustic cell are^{6, 17)}

- (a) microphone of high performance,
- (b) acoustic isolation from the outside,
- (c) minimization of extraneous photoacoustic signal arising from the interaction of the excitation beam with the walls and the windows,
- (d) appropriate cell size to maximizing the acoustic signal within the cell.

Consideration about the above criteria is detailed below.

(a) Photoacoustic cell performance is largely dependent on the microphone used. Both a conventional condenser microphone with external biasing and the electret microphones with internal self-biasing provided from a charged electret foil are sensitive enough to detect the photoacoustic signal. The microphone should not be exposed to high temperatures so as not damage the diaphragm of the microphone unit.

(b) For the purpose of insulating the acoustic noise coming from the outside of the cell, the cell window must have sufficient thickness to form a good acoustic barrier. For sealing the sample room, use of o-rings is preferable. The

backside of the microphone must also be sealed. A pneumatic insulation table or a rubber insulator is preferable for insulating noise from table or floor.

(c) In order to minimize any photoacoustic signal arising from the interaction of the excitation X-rays and scattered X-rays with the walls and the windows, an exit window for the transmitted beam and large cell windows (incident and exit) are necessary. In order to avoid absorption of the scattered excitation beam, the cell body materials are required to have a large heat conductance, large heat capacitance and a low absorption coefficient for the excitation X-ray beam. Aluminum is suitable as a cell material based on these criteria.

(d) Since the signal amplitude is inversely proportional to the gas volume of the sample chamber, the cell must be designed to have a small inner volume. However, care must be taken not to minimize inner volume to the point that the acoustic signal produced at the sample suffers appreciable dissipation to the cell walls through thermo-viscous damping effects. It is also necessary to ensure that energy is not lost to the window directly in front of the sample. The distance between the sample surface and the cell windows should always be greater than the thermal diffusion length of the gas since it is the boundary layer of gas that acts

as the acoustic piston generating the signal in the cell. For air at room temperature and pressure, the thermal diffusion length is about 0.02cm at a chopping frequency of 100Hz. Taking this thermal diffusion length criterion into account and the need to minimize sound energy dissipation to the cell boundaries via the thermo-viscous effect, a minimum distance between sample and window is about 2mm.

Figure 2-1-1 shows the sensitivity *versus* the chopping frequency characteristic of the photoacoustic cell used in this study. In this measurement, a laser diode of 810nm light wavelength and of 200mW output power was used as the excitation source and a black painted paper sheet was used as the light absorber. Photoacoustic signal amplitude at the chopping frequency of 100Hz is $56\mu\text{V/mW}$ and the signal noise ratio is about 370. The signal amplitude decreases with the chopping frequency. But the signal to noise ratio is substantially constant in the frequency range of 10 to 300Hz. The lowest power to hold the signal to noise ratio of 3 is about 0.01mW at the chopping frequency of 100Hz. Therefore, from a practical point of view, the X-ray power is desired to be more than 0.1mW.

2-1-3 Signal Processing System

Signal processing in the photoacoustic measurements can

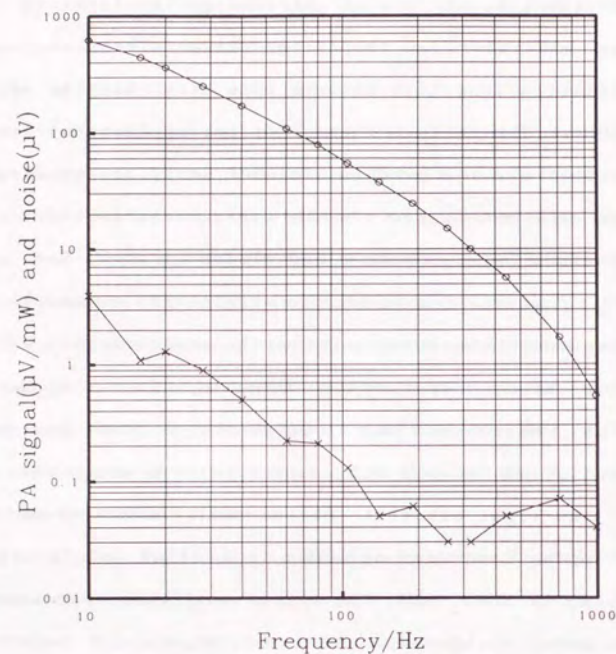


Fig. 2-1-1. Frequency characteristic of a photoacoustic cell with an integration time of 10s.

be performed in many ways. However, certain basic procedures should be followed. Signals from the microphone preamplifier are amplified by a lockin amplifier referred to the chopping frequency. For stable operation of the lock-in amplifier, stability in modulating the exciting source and that of the reference signal are serious problems. A stable motor and precise chopper blade must be used especially when hand made chopper is used. Inaccuracy in the chopper blade causes jitters and instability in the reference circuit of the lock-in amplifier. In order to avoid additional noise, the following care should be taken: The electric ground circuit must not make a loop; the preamplifier must be located near the cell; suitable filters in the signal circuit should be to remove noise in the signal; and electric noise from the digital circuit such as the computer need to be taken care of.

2-2 Photoacoustic Signal Detection under X-ray Tube Excitation

Introduction

Theoretically photoacoustic experiments can be conducted in any wavelength region of excitation. However, it has mostly been conducted in the visible and infrared regions except for a work on X-ray dosimetry¹⁸⁾. Recently photoacoustic experiments in the X-ray wavelength region were successfully conducted with the use of synchrotron radiation as an excitation source¹⁹⁾. In the present study, photoacoustic experiments have been executed without the use of synchrotron radiation, but with the use of a conventional X-ray tube. Experiments using X-ray tubes are easily accessible.

Experimental

A built-in type X-ray tube with a molybdenum target was used as an excitation source in the present experiment. An aluminum blade sector was used for chopping the X-ray beam. The transmittance of the aluminum blade for the Mo-K_{α} radiation was estimated from the mass absorption coefficient and the thickness of the blade (1mm) is considered to be effective for modulation since the remaining 75% of the incident X-ray is chopped by the sector. Figure 2-2-1 shows

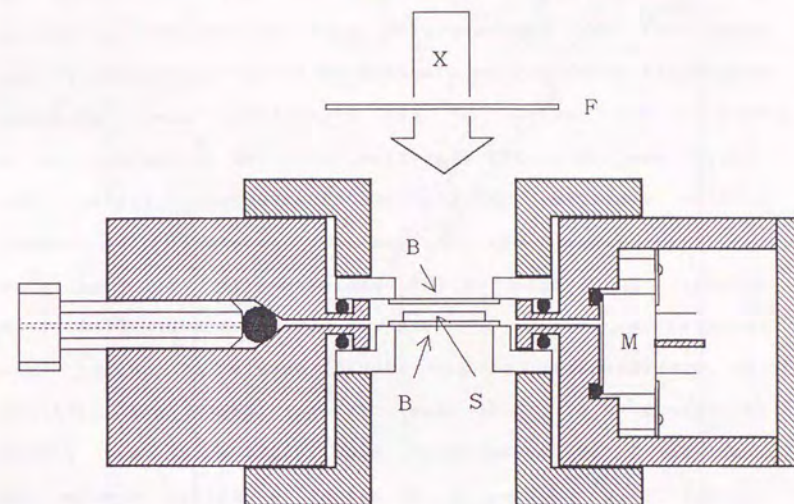


Fig. 2-2-1. Photoacoustic cell for X-ray measurement.

B, beryllium window; S, sample, ● : viton o-ring.

the designed sample cell used for the present experiment. The thickness of each beryllium window (upper and bottom) was 0.25mm. A beryllium filter (0.25mm thick) was placed in front of the photoacoustic cell to eliminate X-ray components which may be absorbed by beryllium window of the cell. The output of the microphone was impedance transformed at an FET amplifier, and then introduced to a lock-in amplifier (NF Electric Instruments, LI575). The amplified signal was recorded on a recorder. The signal without the sample in the photoacoustic cell was also recorded as a background signal, which was subtracted from the photoacoustic output signal. Sheets of copper foil (thickness 0.01, 0.1, 1mm, diameter 13mm) were used as samples. In the measurement, each sample sheet was placed contact face to face on the bottom beryllium window. In order to measure the X-ray spectra of the exciting source, X-rays scattered by a acrylic acid resin plate (5mm thick) were measured using a Si-Li solid state detector (Kevex, model 3200-0190) incorporated in the fluorescent X-ray apparatus.

Result and Discussion

Figure 2-2-2 shows plots of the photoacoustic signal intensity for the 0.01mm copper foil *versus* the X-ray tube current at a chopping frequency of 40Hz. The

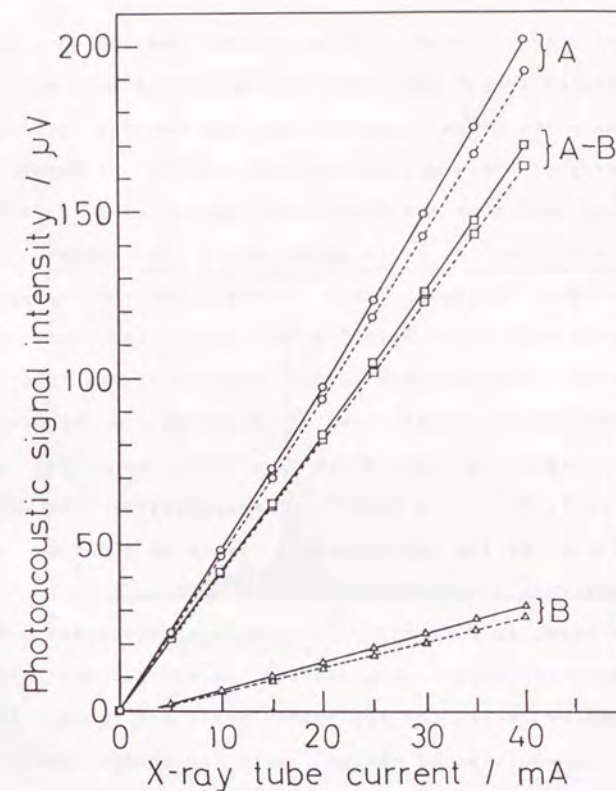


Fig. 2-2-2. Photoacoustic intensities *versus* X-ray tube current. Solid line and dotted line show the intensities of photoacoustic signal detected without and with beryllium filter. A, Direct read; B, background.

photoacoustic signal intensity is considered to be proportional to the exciting X-ray power, because the latter is known to be proportional to the tube current. Taking the efficiency of X-ray generation as 1.7×10^{-3} , the X-ray power generated at 40KV and 40mA is estimated to be $2.7 \text{ W}^{(2)}$. In this estimation k value in eq. 2-1-1 is assumed to be 1×10^{-9} . The incident X-ray energy to the sample is calculated as $2.7 \times 1.3 \times 10^{-3} = 3.5 \text{ mW}$ under the experimental conditions: the distance $l=70 \text{ mm}$ between the Mo target and the sample, the radius $r=5 \text{ mm}$ of the beryllium window, the steric angle of the X-ray radiation on the sample $(1/4\pi)(\pi r^2/l^2) = 1.3 \times 10^{-3}$. Consequently, the signal sensitivity of the photoacoustic cell with a 0.01mm copper foil sample is found to be 43 mV/W .

As shown in Fig. 2-2-2, the background intensity of the photoacoustic signal detected for the sample cell without any samples were not negligibly small and about 15% of signal intensities of the cell with the copper sample. The background is considered to be due to absorption of the excitation beam by the cell window and the cell wall. There are two possibilities for cell wall absorption of cell. One is absorption of the direct excitation beam, the other is absorption of scattered beam by the cell body and the cell window. Figure 2-2-3 shows the X-ray spectra of the excitation source and transmittance through the beryllium

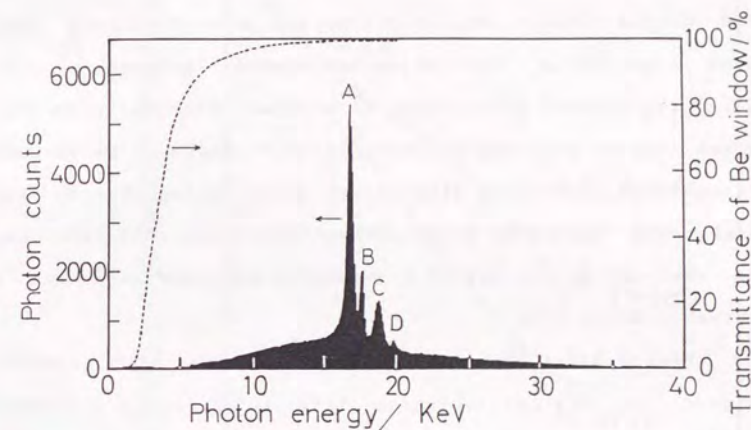


Fig. 2-2-3. X-ray spectra of excitation source and transmission spectra of beryllium window of 0.25mm thickness (dotted line).

A, compton scattering peak of Mo K_{α} ,
C, compton scattering peak of Mo K_{β} ,
B: Mo K_{α} , and D: Mo K_{β} .

window (0.25mm thick)²⁰⁾. The spectra shows that the exciting source contains a low energy component which can be absorbed by the beryllium window. The origin of the background is expected to be absorption of the excitation beam by the beryllium window and by the sample cell wall. The dotted lines in Fig. 2-2-2 were signals from the cell with a beryllium filter which was placed in front of the beryllium window. This filter eliminates the X-ray component which may be absorbed by the beryllium window. Background intensities decreased slightly as shown in Fig. 2-2-2. The background caused by X-ray absorption in the cell wall may be reduced by the use of a carefully designed cell and a suitable X-ray slit.

Figure 2-2-4 shows the dependence of the photoacoustic signal on various chopping frequencies. The thermal diffusion length μ_s , which is defined as $\mu_s = 2k/c\rho\omega$ with k the thermal conductivity, ρ the density, c the specific heat, and ω the angular chopping frequency, is calculated to be 1.9mm at $\omega=2\pi\times 10$, and 0.5mm at $\omega=2\pi\times 120$ for the copper sample using the values of $k=0.923\text{cal cm}^{-1}\text{s}^{-1}\text{C}^{-1}$, $c=0.0919\text{cal g}^{-1}$, and $\rho=8.93\text{g cm}^{-3}$. The optical penetration length $\mu_\beta (=1/\beta)$ of the copper sample for Mo-K α characteristic X-ray radiation is calculated to be 0.022mm with an absorption coefficient of $\beta_m=0.504\times 10^2\text{ cm}^2\text{ g}^{-1}$ and ρ . Consequently, the 0.01mm thick foil sample is optically

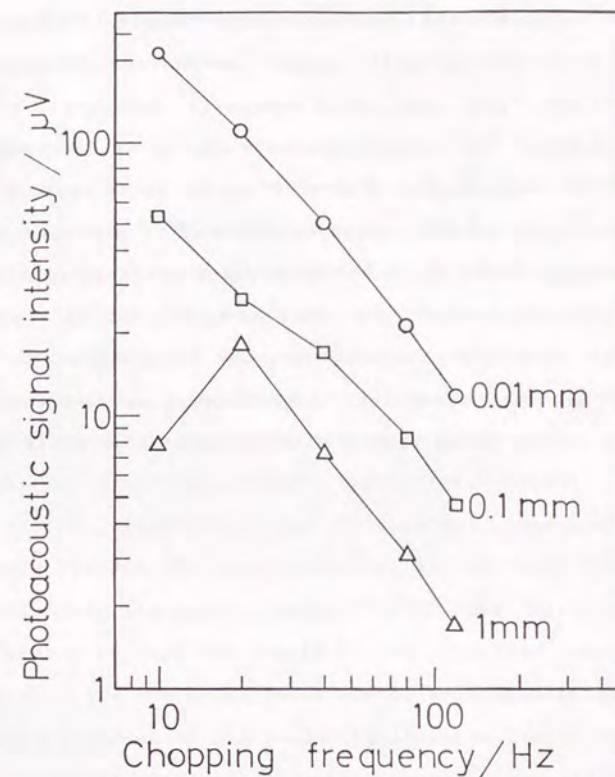


Fig. 2-2-4. Photoacoustic intensities *versus* chopping frequency.

and thermally transparent, while those of 0.1mm and 1mm thickness are optically opaque but thermally transparent at $\omega=2\pi\times 20$. The 1mm thick sample is thermally opaque at $\omega=2\pi\times 120$. The signal intensity has an approximate ω^{-1} - $\omega^{-1.15}$ dependence (Fig. 2-2-4), which is consistent with the theory of Rosencwaig and Gersho⁷³. The sample of 1mm thickness shows an $\omega^{-1.4}$ dependence at chopping frequencies larger than 20Hz. This seems to be due to the intermediate state between a thermally thin and thick case.

It was shown that photoacoustic measurements can be done in the X-ray region with the use of an X-ray tube.

2-3 Detection of Photothermal Deflection Signals with X-ray Excitation

Introduction

Measurements based on photothermal effects in the X-ray region have been conducted in the field of X-ray photoacoustic spectroscopy (X-ray PAS)¹⁸³. The photoacoustic method is known as one of the detection techniques associated with the photothermal phenomenon. It detects the pressure deviation in a photoacoustic cell containing the sample with, for instance, a microphone as the transducer. The photothermal deflection method is another detection technique of the photothermal phenomenon, where signals are detected as deflections of the probe beam which grazes along the sample surface^{21, 22}. The advantage of this method is that the sample is not required to be sealed in the cell, so there is no sample size limitation. Additionally, experiments are nondestructive and can be made in remote location. Further, with this method, experiments in the soft X-ray region and those where the X-ray beam incident with a small angle can be easily conducted. In these conditions, absorption and occultation of the excitation beam by the window will be a problem in photoacoustic measurements.

Experimental

The experiment was conducted using the synchrotron radiation X-ray beam (the beam-line BL-15A at the National Laboratory for High Energy Physics, Tsukuba, Ibaraki) as an excitation source. Figure 2-3-1 shows the schematic diagram of the experimental setup. The X-rays were monochromated at 0.15nm and chopped by a mechanical sector blade. The beam was focused on the sample surface with a cylindrical mirror of fused quartz. The cross section of the beam was about 8mm in length and 2mm in width at the sample surface. A helium-neon laser (2mW, 05-LHP-321, Melles Griot, U.S.A.) was used as a probe beam source. Deflection of the probe beam was detected by a position sensitive detector PSD (S1545, Hamamatsu Photonics, Japan), with necessary peripherals. The PSD was set 30cm from the sample. The photothermal deflection signal was preamplified (x100) at the beam site and then led out of the experimental hutch room for later signal processing. The preamplified signal was introduced into a lock-in amplifier (LI575, NF Circuit Design Block Co. Ltd., Japan), the outputs of which, both in amplitude and phase, were recorded on a chart and also stored in a computer (PC9801, NEC, Japan). Sheets of copper foil (thickness 20 μ m and diameter 18mm) and molybdenum foil (thickness 100 μ m and diameter 18mm) were used as samples. They were adhered on a foaming polystyrene plate (thickness

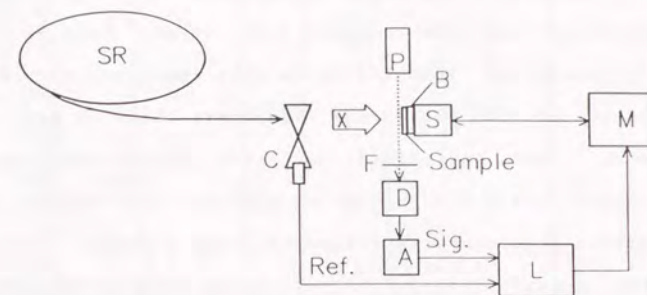


Fig. 2-3-1. Schematic block diagram of photothermal deflection measurement by X-ray excitation.
SR, synchrotron ring; X, chopped X-ray beam; C, chopper; P, He-Ne laser (2mW); M, micro-computer; B, polystyrene foam base; S, XZ-stage; F, filter; D, position sensitive sensor with peripherals; A, preamplifier (x100); L, lock-in amplifier. Probe beam is shown with a dotted line.

about 5mm) and mounted on an XZ-stage.

Results and Discussion

Figure 2-3-2 shows the photothermal deflection signal detected for the copper foil sample with a chopping frequency of 15Hz and an integration time of 12.5s. The noise of the background signal was about $0.5\mu\text{V}$ peak to peak, and the signal to noise ratio was about 50. Figure 2-3-3 is a log-log plot of the signal intensity versus the chopping frequency f for a copper foil sample. The signal intensities were normalized to the X-ray beam intensity which was measured by an ion chamber placed in front of the sample. As seen in Fig. 2-3-3, the signal intensity shows the f^{-1} dependency with respect to the chopping frequency f . According to Murphy and Aamodt,²²⁾ the f^{-1} dependency should correspond to the case where the sample is "thermally thin" and the probe beam offset, which is defined as the distance between the beam center and the sample surface, has a comparable order of magnitude to the thermal diffusion length μ of air defined as $\mu = (k/\pi c f \rho)^{1/2}$ with the thermal conductivity k , the specific heat c and the density ρ . The conditions of the present experiment are considered to agree with these criteria.

Since copper is a good heat conductor ($k=398\text{Wm}^{-1}\text{K}^{-1}$)

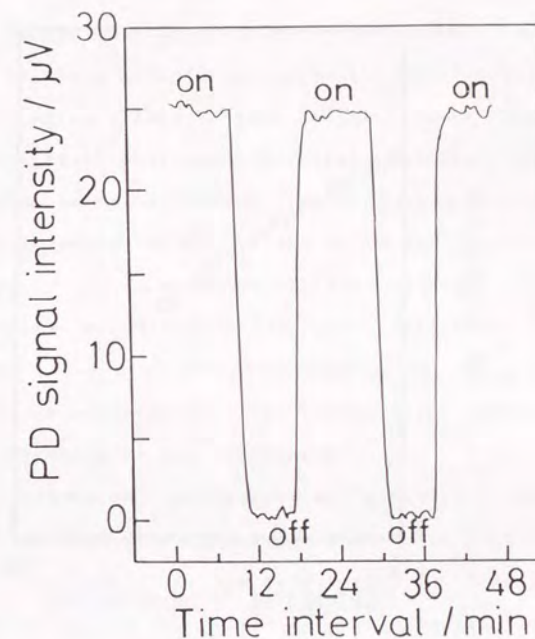


Fig. 2-3-2. Photothermal deflection signal intensity recorded on a chart recorder for a copper foil sample with an integration time of 12.5s and the parallel optical arrangement.

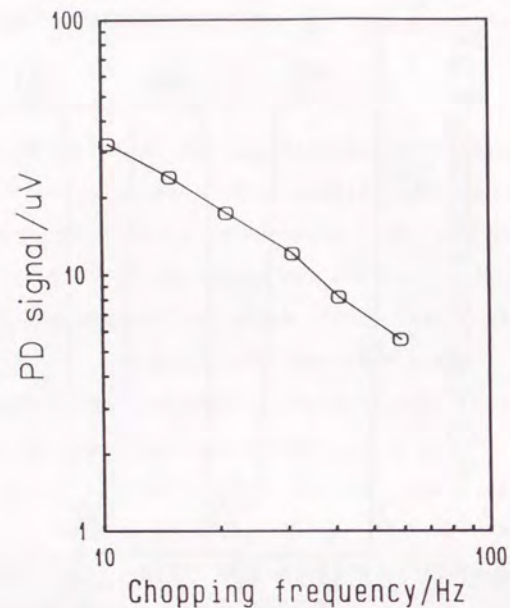


Fig. 2-3-3. Photothermal deflection signal intensity vs. chopping frequency.

and the sample thickness is $20\mu\text{m}$, the copper sample is regarded as belonging to the thermally thin case in the frequency region $f=10.4$ to 60Hz of the present experiment. The beam offset was adjusted approximately to 0.5mm . Further, the thermal diffusion length μ_{air} is calculated to range from approximately 0.75 to 0.3mm for chopping frequencies f in the range of 10.4 to 60Hz using the reported values $k=2.41 \times 10^{-2} \text{Wm}^{-1}\text{K}^{-1}$, $c=1.006 \times 10^3 \text{Jkg}^{-1}\text{K}^{-1}$ and $\rho=1.293 \text{kgm}^{-3}$ for air. The calculated value μ_{air} is thus considered as comparable to the beam offset, resulting in the f^{-1} dependency in our experiment.

Two geometrical arrangements, "parallel" and "small angle reflection" arrangements, for the probe beam with respect to the sample surface were tested for detecting the beam deflection. In the "parallel" arrangement, the probe beam which is grazing along the sample surface directly impinges on the PSD. On the other hand, in the "small angle reflection" arrangement, the probe beam is irradiated onto the sample surface with a small angle of incidence and then reflects, at the spot of the excited surface, towards the PSD. In the latter arrangement, the PSD should be placed so as not to receive the direct probe beam. The angle of incidence was about one degree with respect to the sample surface in this experiment. These two arrangements were attempted to detect the beam deflection signal for a

molybdenum foil sample. Figure 2-3-4 shows the signal intensities for the molybdenum sample. As seen in Fig. 2-3-4, the parallel arrangement was better and recommended as far as signal to noise ratio was concerned, although it was somewhat more difficult in setting the sample and the probe beam in an optimal arrangement.

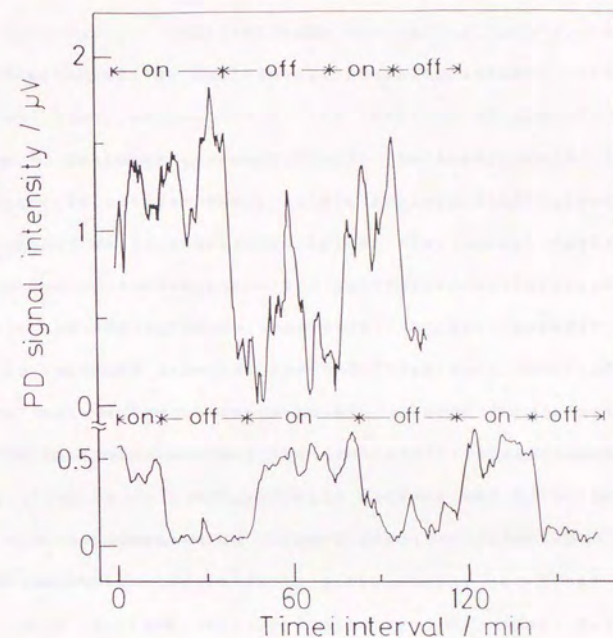


Fig.2-3-4. Photothermal deflection signal intensity recorded on a chart recorder. The upper trace was the result for the small angle reflection arrangement and the lower trace was for the parallel arrangement for a molybdenum foil sample.

CHAPTER III

Correlation Photoacoustics in the X-ray Region

Photoacoustic spectroscopy combined with the correlation technique yields a new aspects of photoacoustics in the sense of i) direct delay time measurement of photoacoustic output and ii) non-destructive measurement of a layered sample. This section 3-1, which is based on published reports,^{23, 24)} introduces fundamentals of the correlation method and examples in which the correlation photoacoustics technique was successfully applied to model samples in the visible light region.

Correlation photoacoustic spectroscopy was carried out in the X-ray region using synchrotron radiation (SR) and an X-ray tube as excitation sources. Section 3-2, which is based on a published report,²⁵⁾ presents an investigation about thermal diffusion in copper foils and in laminated samples. The characteristic rise and fall times of correlation spectra, τ_0 and τ_f , respectively, were found to be influenced by sample thickness. For laminated samples, thermal resistance of the surface layer was obtained from the characteristic fall time of the impulse response. Section 3-3, which is also based on a published report,²⁶⁾ presents an investigation about observations of a layered structure. Two peaks with different delay times were

observed separately. The first and the second peaks were considered to be related to the heat from the surface layer and the deep layer, respectively. The interval of the first and the second peak was proportional to the thickness of the surface layer. It was found that the intensity of the second peak was influenced by the optical properties of the surface layer. For laminated samples of polymer and lead foil, the signals from an intermediate lead layer can be observed in addition to signals from the surface layer and deep lead layer. Section 3-4 presents correlation spectra near the absorption edge where the depth of heat generation changes with excitation wavelength. It was found that the peak intensity and the characteristic fall time were changed with the excitation wavelength.

3-1 Correlation Photoacoustics

Introduction

In photoacoustic spectroscopy, it is well known that the photoacoustic signal shows a time delay with respect to the excitation signal. The delay of the output signal comes from various contributing factors, such as non-radiative relaxation from the excited state, thermal diffusion, propagation of the acoustic wave, etc., and thus offers various information about a given sample²⁷⁾. If the conventional lock-in amplifying technique with the use of a regular chopping technique is used, the time delay of the output signal is observed as a delay in the phase angle, which depends on the modulation frequency ω ^{8, 28)}. Problem with the lock-in amplifying method lies with absolute measurement of the phase delay and measurements must be done at many chopping frequencies. Moreover, if the output signal contains more than two components having different delay times, they are only observed as a composite signal both in phase and amplitude so that they cannot virtually be separated into each component.

Another way to measure the signal delay is measuring the impulse response for an impulse excitation. But, the impulse excitation has disadvantages such as i) impulse source is not easily accessible (especially in the X-ray

region), ii) low efficiency of available energy when a continuous source is used as a pulsed source with the use of a shutter, iii) susceptibility to the noise emitted from the impulse source, iv) saturation and damage of sample due to the large peak power of the impulse excitation. Introduction of the correlation technique^{29, 30)} into the signal processing in place of the pulsed excitation makes it possible to obtain the delay time of the output signal in the form of a mathematical impulse-response function of the system without any use of pulse excitation. This is based on a theorem^{31, 32)} that the cross-correlation between a random input signal and the resultant output signal equals the impulse-response function of a linear system. This method also enables one to obtain the photoacoustic spectra of each layer of a layered sample without separating it prior to the experiment. In this chapter we discuss the case where the time delay arises only from the thermal diffusion process in the sample, and present the correlation photoacoustic spectra of the first and the second kind of model samples.

Principle of Method

Figure 3-1-1 is a block diagram of the measuring system for correlation photoacoustic spectra in the visible light region²³⁾. The excitation beam was chopped by a mechanical

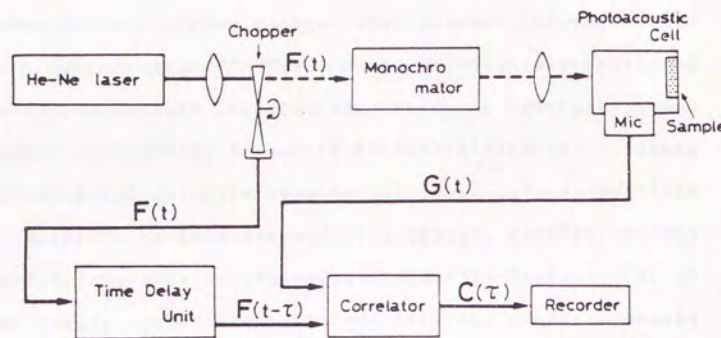


Fig. 3-1-1. Block diagram showing the measuring system of correlation photoacoustics. With the measurements in X-ray region, the He-Ne laser and monochromator is replaced by an X-ray source such as X-ray tube or synchrotron radiation (SR).

"pseudo-random chopper" and was irradiated onto the sample. The photoacoustic output signal $G(t)$ was detected by a microphone as a time dependent signal and was introduced into the correlator. The reference signal $F(t)$, which was detected by a photo-coupler installed in the chopper or photosensor placed in the beam flux, was lead to the TDU (Time Delay Unit) which generated the time-delayed reference signal $F(t-\tau)$ and then introduced to the correlator. The output signal $C(\tau)$ of the correlator was recorded as a function of delay time τ . The TDU circuit was laboratory made with the use of a commercially available microcomputer kit (NEC, TK-80) with necessary peripheral units added. The time delay unit and the correlator can be replace by a digital FFT analyzer.

Generally the correlation function $C(\tau)$ between $F(t)$ and $G(t)$ is explicitly given as

$$C(\tau) = \lim_{T \rightarrow \infty} \frac{1}{2T} \int_{-T}^T F(t-\tau) G(t) dt, \quad (3.1.1)$$

where $2T$ is the integrating time span. In practice, it was adjusted to be long compared to one cycle of the pseudo-random series and became about 5-10s as a time constant at the correlator. The functions $F(t)$ and $G(t)$ in equation (3.1.1) are regarded as the input and output functions,

respectively, of the photoacoustic cell with a microphone and the sample. As the input signal $F(t)$ is randomly modulated in time sequence with the use of pseudo-random chopper, the correlation function $C(\tau)$ thus obtained from $F(t)$ and $G(t)$ should be equal to an impulse-response function of the system. The output function $g(t)$ of the system is generally given as a convolution of input function $f(t)$ and the impulse response function $h(t)$ of the system,

$$g(t) = \int_{-\infty}^{\infty} f(t-x) h(x) dx. \quad (3.1.2)$$

The cross correlation function $C_{fg}(\tau)$ of input $f(t)$ and output $g(t)$ is given as

$$C_{fg}(\tau) = \lim_{T \rightarrow \infty} \frac{1}{2T} \int_{-T}^T f(t-\tau) g(t) dt. \quad (3.1.3)$$

Substituting (3.1.2) into (3.1.3),

$$\begin{aligned} C_{fg}(\tau) &= \lim_{T \rightarrow \infty} \frac{1}{2T} \int_{-T}^T f(t-\tau) \int_{-\infty}^{\infty} f(t-x) h(x) dx dt, \\ &= \lim_{T \rightarrow \infty} \frac{1}{2T} \int_{-\infty}^{\infty} \int_{-T}^T f(t-\tau) f(t-x) dt h(x) dx, \end{aligned}$$

$$= \int_{-\infty}^{\infty} C_{ff}(\tau-x) h(x) dx, \quad (3.1.4)$$

where $C_{ff}(\tau-x)$ is the auto correlation function of $f(t)$. The input function $f(t)$ is a random function, therefore the auto correlation function of $f(t)$ becomes a Dirac's delta function $C_{ff}(\tau) = \delta(\tau)$, so that we finally obtain

$$\begin{aligned} C_{fg}(\tau) &= \int_{-\infty}^{\infty} \delta(\tau-x) h(x) dx, \\ &= h(\tau). \end{aligned} \quad (3.1.5)$$

If the system has a time delayed response, the impulse response function $C(\tau)$ will give its maximum peak at $\tau = \tau_0$ which corresponds to the delay time of the output $G(t)$ with respect to the input $F(t)$, the excitation signal (Fig. 3-1-2). $C(\tau)$ curve obtained in this way are defined as the correlation photoacoustic spectra of the first kind.

While the correlation photoacoustic spectra of the first kind are recorded as a function of delay time τ at a constant excitation wavelength λ , the correlation spectra of the second kind are defined as those recorded as a function of excitation wavelength λ at a fixed delay time τ_D .

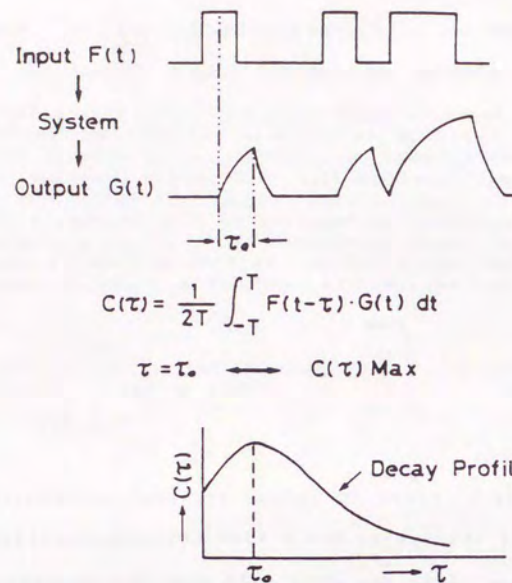


Fig. 3-1-2. Diagram showing the relation of the input $F(t)$, the photoacoustic output $G(t)$ and the correlation function $C(\tau)$ with the maximum peak at $\tau = \tau_0$, as indicated by the delay time τ_0 of $G(t)$ with respect to $F(t)$.

Random Chopper

It is desired that the excitation source in correlation photoacoustics be random in nature. The system for generating an ideal random modulation is a complicated and costly one. A convenient way of generating a random modulation is where one uses a mechanical chopper based on the M-series (maximum-length linear shift register sequence) pseudo-random binary sequence³⁰. By the use of the chopper with M-series sequence of suitable length and rotating speed, i) one can obtain satisfactory randomness in the practical frequency range; and ii) signal processing is easily conducted owing to the binary nature of the sequence. A silhouette of the pseudo-random chopper for period $n=127$ ($=2^7-1$) is shown in Fig. 3-1-3 together with the employed binary sequence of "0" and "1". The power spectrum of the chopper is also given in Fig. 3-1-3. Ideal resolution of the measuring system depends on the revolving speed of the chopper and number of on-off units contained in a cycle of the chopper blade. The highest component in the power spectrum in Fig. 3-1-3 is about 1450Hz, which corresponds to a time resolution of about 0.7ms.

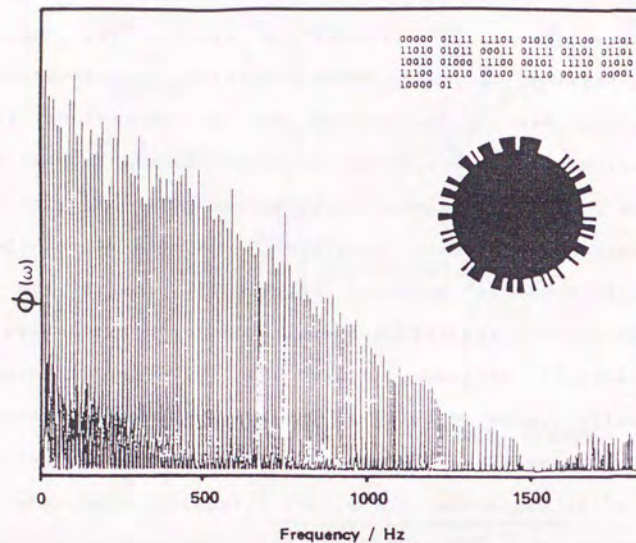


Fig. 3-1-3. Silhouette of a random chopper based on an M-series binary sequence ($n=127$). The M-series binary sequence and power spectrum of the random chopper are also shown.

Correlation Photoacoustic Spectra of the First Kind (Relation between the Depth of Heat Generation and the Delay Time τ_0)

As mentioned before, the delay time τ_0 are obtained directly from the peak position in the correlation photoacoustic spectra of the first kind. The factors which will contribute to the delay time τ_0 are i) the relaxation time of the sample; ii) propagation delay of the heat pulse generated in a deep layer to reach the sample surface by conductive diffusion; iii) time delay at the surface where the thermally diffused heat is converted into acoustic energy.

In the present study we will consider only the case where the delay time τ_0 is dominated by thermal diffusivity in the sample, while other contributions are considered negligible to a good approximation. In such a case, the depth of heat generation in the sample and the signal delay time τ_0 is expected to have a definite relation which should be experimentally determined.

Figure 3-1-4a. shows a model sample I which consists of the light absorber of blue paint spread on a glass plate and is coated by sheets of polyethylene films. Each film of about $15\mu\text{m}$ in thickness was piled up in layers so as not to contain air bubbles in between. The irradiating light from the 50mW He-Ne laser penetrates through the polyethylene

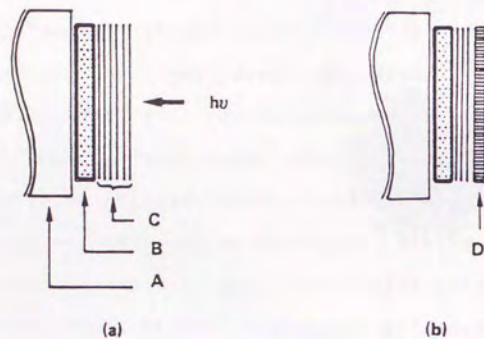


Fig. 3-1-4. Model samples I and II with a layered structure: model sample I (a), a light absorbing layer of blue paint (B) lies on a glass plate (A) and at the bottom of the sheets of polyethylene film (C), model sample II (b), an additional absorbing layer of enamel (D) is placed upon the surface sheet of the polyethylene film.

films and is absorbed by the blue paint, where the absorbed energy is converted into heat. The heat diffuses to the sample surface through the films and is converted to acoustic energy at the surface of the polyethylene film. The polyethylene film is transparent in the visible range (250-800nm) so that no heat generation is expected to occur in the films. Thus τ_0 value obtained from the first kind correlation photoacoustic spectra is considered to be dependent only on the film thickness. Figure 3-1-5 shows some representative of the first kind spectra and Fig. 3-1-6 shows the plots of the delay time τ_0 versus the thickness of film sheets for model sample I. The peak width became broader and of less time resolution since the heat propagates as it diffused through the material.

Correlation Photoacoustic Spectra of the Second Kind.

The correlation output is a function of wavelength λ as well as delay time τ . For simplicity, the delay of the photoacoustic signal is supposed to arise mainly from the delay due to heat diffusion in the sample. If the correlation output is recorded as a function of the wavelength λ of the irradiating light at a fixed delay time τ_D , the obtained curve will correspond to the photoacoustic spectra from a layer which lies at a certain depth below the surface. This spectra is defined as the

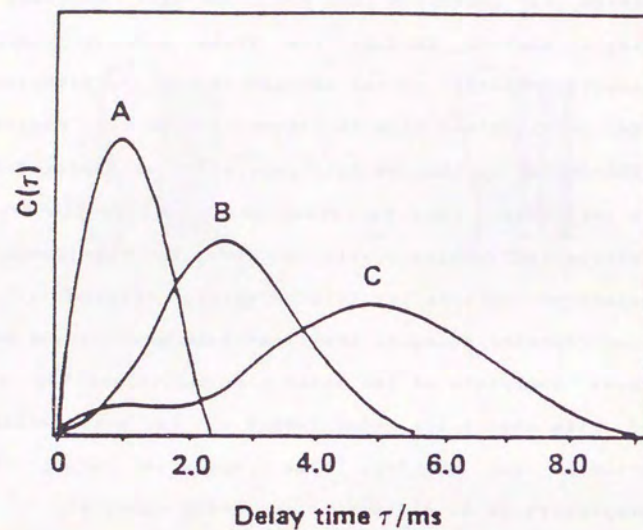


Fig. 3-1-5. The first kind correlation photoacoustic spectra of model sample I with a polyethylene film of $0\text{ }\mu\text{m}$ (A), $30\text{ }\mu\text{m}$ (B) and $60\text{ }\mu\text{m}$ (C) thickness.

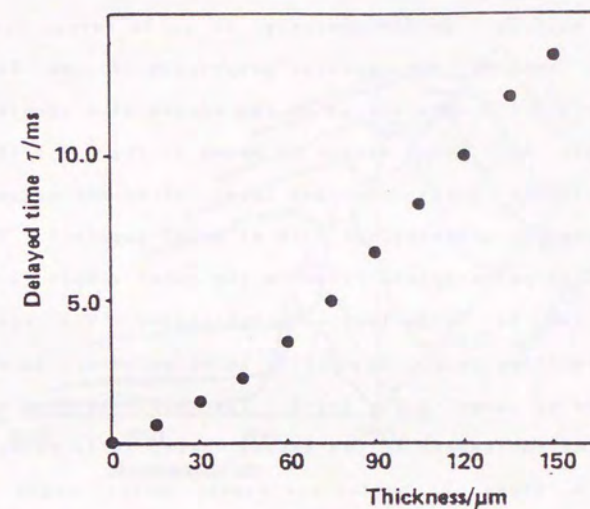


Fig. 3-1-6. Plots of the delay time τ_0 of model sample I as a function of polyethylene film thickness.

correlation spectra of the second kind. If τ_D is small, the spectra will reflect information about the layer near the surface. On the contrary, if τ_D is large, the spectra will reflect the optical properties of the deep layer. Figure 3-1-7 show curves of the second kind spectra of model sample II. Model sample II shown in Fig. 3-1-4b. has an additional light absorber layer of enamel spread on the uppermost polyethylene film of model sample I. The number of the polyethylene films in the model sample II was fixed to two for experimental convenience. The axis of the correlation output $C(\tau, \lambda)$ is taken as normal to the $\tau\lambda$ -plane as shown in Fig 3-1-7. The peaks observed at lower λ region correspond to the enamel layer, while those observed at a higher λ region correspond to the light absorbing layer of the blue paint at deeper levels. The highest enamel peak appears at a small τ_D value of approximately at 1.0ms, while that of the light absorber appears at a larger τ_D value of about 3.0ms. The relation between the first kind and the second kind spectra will be clearly understood if the curves of Fig. 3-1-7 are cut by a plane parallel to the τ C-plane. The cross section thus obtained at certain wavelength λ will give the first kind spectra irradiated at wavelength λ .

It appears that the correlation photoacoustic spectroscopy offers a convenient method for obtaining

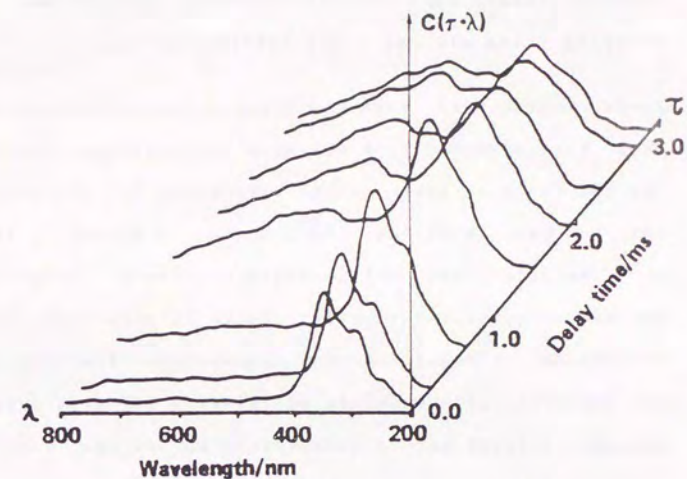


Fig. 3-1-7. Curves of the second kind correlation photoacoustic spectra of model sample II. Correction of the power spectrum of the excitation source (Xe lamp) is not made in the spectra.

information about the thermal and optical properties of layered solids, such as semiconductors, photofilms, paints, wrapping films etc. in a non-destructive way.

3-2 Correlation Photoacoustic Measurement by Excitation with Synchrotron Radiation (Thermal Properties)

Introduction

Photoacoustic measurement provides information about the thermal properties of bulk and layered materials non-destructively⁶⁾. In the photoacoustic study in X-ray region, elemental analysis would be possible using the characteristic X-ray absorption for each element. In addition, introduction of the cross correlation technique into photoacoustic measurement provides further information about materials. The correlation photoacoustic technique has two features: one is the measurement of the impulse response characteristics of a sample caused by absorption of photons, and the other is that of time resolved spectra. These are referred to as the first and the second kind of correlation photoacoustics^{24, 33)}. Spectra of the first kind provides information on the thermal and structural properties of the sample material³⁴⁾. In the present experiments, the delay time τ_0 is dominated by the sample thermal diffusivity. Contributions to τ_0 from other sources such as deexcitation or propagation process of the acoustic wave are considered to a good approximation as negligible here. Although the conventional photoacoustic method gives similar information by use of the phase delay technique^{6, 7)}, the cross

correlation method gives more detailed and straightforward information than the conventional one for understanding the thermal properties of samples.

This section presents an attempt of correlation photoacoustic measurement of copper foil and layered samples in the X-ray region.

Experimental

Figure 3-2-1 is a schematic diagram of the experimental arrangement. The experiment was made at beam lines BL-4A and BL-15A at the Photon Factory (National Laboratory for High Energy Physics, KEK, Tsukuba). The X-rays were monochromated to 1.37Å (BL-4A) and 1.48Å (BL-15A) and were focused to a 3mmx2mm area on the samples. A mechanical random chopper containing two M-series ($n=31$) pseudo-random binary sequence (PRBS) was used to modulate the beam. The chopper speed was varied from 1 to 8rps (rotation per second). Figure 3-2-2 shows the photoacoustic cell used. The cell was made of brass with beryllium windows (10mm diameter and 0.25mm thick). The photoacoustic signal was detected by a condenser microphone and was preamplified at the beam site. The amplified signal was introduced into a signal analyzer (SM2100C, IWATSU Electric Co. Ltd.), where the cross correlation between photoacoustic signal and reference signal was calculated and integrated 100 or 400 times. The

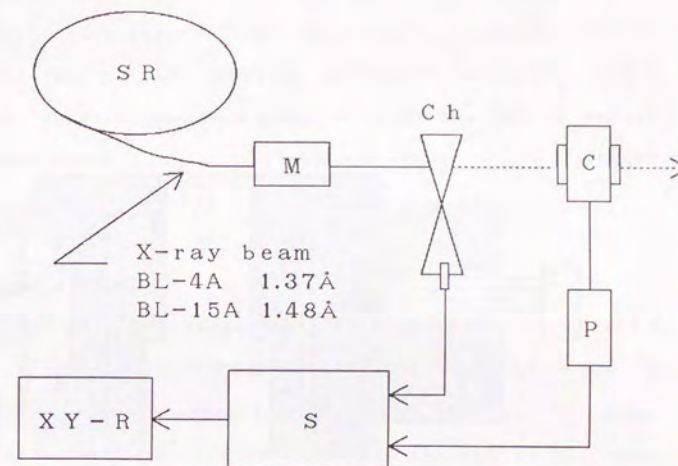


Fig. 3-2-1 Schematic diagram of the experimental arrangement.

SR, synchrotron radiation source; M, monochromator;
Ch, M-series random chopper; C, photoacoustic cell;
P, preamplifier; S, signal processor;
XY-R, XY-recorder.

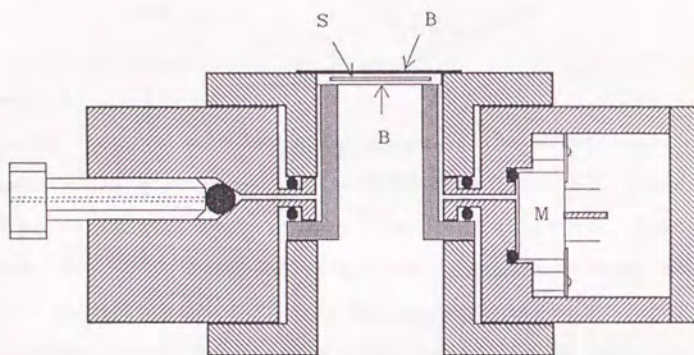


Fig. 3-2-2 Cross section of the photoacoustic cell designed for measurements in the X-ray region. S, sample; B, beryllium windows; M, condenser microphone; ●, O-rings.

reference signal was obtained at an optical coupler installed at the chopper. Sheets of copper foil (thickness 1 to $300\mu\text{m}$ and diameter 10 to 15mm) and laminated sheets of copper foils and adhesive tapes were used as samples. In the case of the latter samples, polymer adhesive tapes (thickness about $50\mu\text{m}$) were adhered on both sides of copper foil (thickness $100\mu\text{m}$, diameter 18mm). The signal intensities were normalized to the ring current.

Results and discussion

Figure 3-2-3 shows the first kind correlation photoacoustic spectra of the copper foil with thickness of $10\mu\text{m}$ for 100 times integration. τ_0 is defined as the time difference between the rising point and the top of the peak, while τ_r is defined as that between the top and the half height point. Since the relaxation time from the excited levels is known to be negligibly short in the X-ray region, τ_0 and τ_r are considered to reflect directly the thermal process of the sample in the photoacoustic cell. τ_A is the full width at half maximum (FWHM) of an auto correlation spectra of the reference signal, so that it should taken as a measure of the time resolution of the measuring system. In the present experiment, the factors which influence the time resolution are the rotating speed of the chopper and the length of the M-series PRBS. Figure 3-2-4 shows the

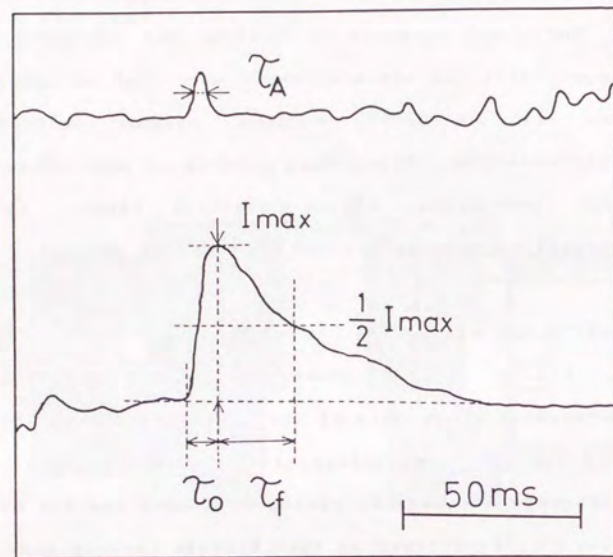


Fig. 3-2-3 The first kind correlation spectra of a $10\text{ }\mu\text{m}$ thick copper foil sample (bottom). Top curve is the auto-correlation of reference signal. τ_A , τ_o , τ_f and I_{\max} are defined in the text.

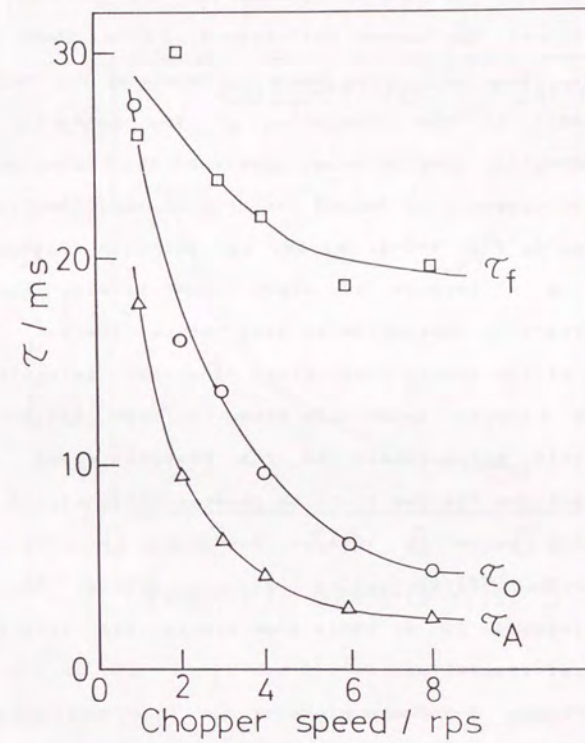


Fig. 3-2-4 Dependence of τ_A , τ_o and τ_f on chopper speed for a $10\text{ }\mu\text{m}$ thick copper foil sample.

dependencies of τ_o , τ_f and τ_A on various chopper speeds for the copper foil sample. τ_o is about 2 times larger than τ_A . This means the measured τ_o values are dependent on the resolution of the measuring system. Consequently, precise measurements of the rising shape of impulse response is beyond the present experimental system. As seen in Fig. 3-2-4, τ_f and τ_o approach constant values with a difference of about 17ms between them. This difference is considered to show the net thermal relaxation time of the sample foil. Plots of signal intensity, I_{max} , versus chopper speed are shown in Fig. 3-2-5. I_{max} is inversely proportional to the chopper speed. This is analogous to the way that the photoacoustic signal in normal chopping shows an inverse dependence on the chopping frequency. This implies that an intense SR beam is advantageous as an excitation source for attaining high temporal resolution.

Figure 3-2-6 are plots of τ_f , τ_o and I_{max} versus sample thickness at a constant chopper speed (4rps). τ_o and τ_f show maximum values at sample thicknesses of 50 and $10\mu\text{m}$, respectively, and then decrease with increasing thickness. The X-ray penetration depth of copper (1.37\AA) is calculated to be about $4\mu\text{m}$, as calculated from the mass absorption coefficient $280\text{cm}^2\text{g}^{-1}$ and density 8.93gcm^{-3} . The copper samples used in this experiment were optically

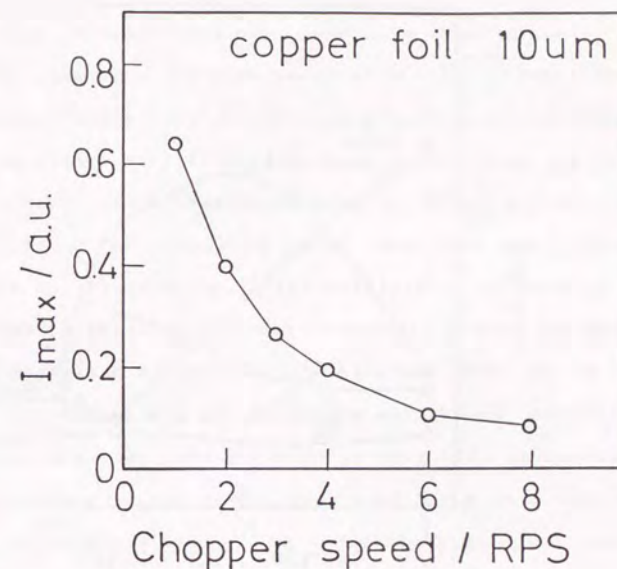


Fig. 3-2-5 Dependence of I_{max} on the correlation spectra of a $10\mu\text{m}$ thick copper foil sample on chopper speed.

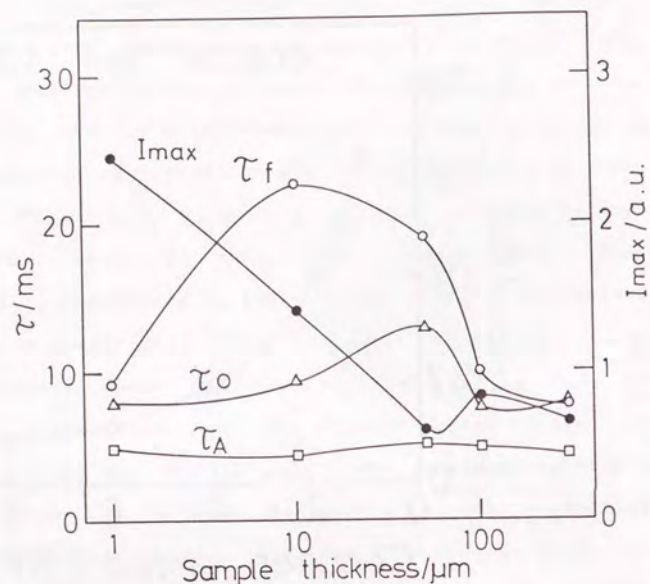


Fig. 3-2-6 Changes of τ_o , τ_A , τ_f and I_{\max} of correlation spectra of copper samples versus sample thickness.

thick except for the sample of $1\mu\text{m}$ thickness. In the samples with a thickness larger than the optical penetration depth, heat dissipation may occur in the process of diffusion, causing a rapid decrease of surface temperature. In the cases where dissipation is negligible, τ_f shows a monotonous change with increasing sample thickness, as seen for the case of the laminated sample (Fig. 3-2-7). The decrease of τ_f for the thick copper sample in the present experiment is probably due to the dissipation of heat in the sample. The decrease of τ_o with increasing sample thickness can be explained as follows: for samples with large τ_o values, the temperature of the sample surface is maintained relatively high for long periods, so that the heat supply from the surface to the air is continued for a long period, causing an increase of τ_o . On the other hand, the small heat capacity for the $1\mu\text{m}$ thick sample explains the short τ_f and the large I_{\max} .

Figure 3-2-7 are plots of τ_o , τ_f and I_{\max} as a function of the number of adhesive tape layers for laminated samples at constant chopper speed (4rps). τ_o and τ_f show a monotonous increase with the number of tape layers. The increasing τ_o values shows the increased delay of the generated heat to diffuse to the surface of the sample through the tapes. The increased τ_f and the decreased I_{\max} reflect the increased heat resistance between the copper

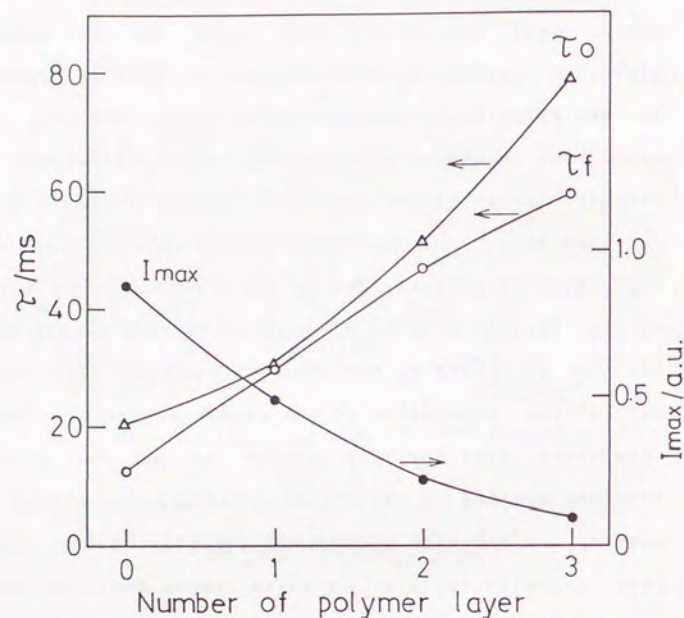


Fig. 3-2-7 Changes of τ_o , τ_f and I_{max} for laminated samples versus the number of adhesive films placed on the substrate.

layer and the inner atmosphere of the sample cell by adhering the tapes on the copper layer. Referring to thermionics, the time constant τ_t of thermal relaxation is calculated as $\tau_t = RC$, where R and C are the heat resistance and the heat capacity of the sample³⁶⁾ respectively. τ_t is related to τ_f as $\tau_f = 0.692 \tau_t$. Therefore the heat resistance and the heat capacity can be easily obtained as $R = \tau_f / (0.692C)$ and $C = \tau_f / (0.692R)$. In this experiment, C can be given as $3.45 \times 10^{-2} \text{ J K}^{-1} \text{ cm}^{-2}$ with the values of specific heat capacity $24.5 \text{ J K}^{-1} \text{ mol}^{-1}$, density 8.96 g cm^{-3} , atomic weight 63.55 g mol^{-1} ³⁶⁾, and thickness 0.01 cm . R values for laminated samples are calculated to be 0.51 , 1.25 , 1.95 and $2.47 \text{ J}^{-1} \text{ K s cm}^2$ using τ_f values of 12.2 , 29.8 , 46.7 and 59.1 ms . Thermal characteristics for surfaces can thus be easily measured by using the X-ray correlation photoacoustic technique.